Technische Universität Wien

Fakultät für Physik

# DIPLOMARBEIT

# Investigation on Chirped Frequency Combs from a Frequency-Shifted Feedback Ti:Sapphire Laser seeded by a Phase-modulated Single-frequency Fiber Laser

ausgeführt am

Institut für Photonik der TU Wien

unter der Leitung von

Univ.Prof. PhD. Andrius Baltuška
Dr. Oliver D. Mücke

durch

**Dipl.-Ing. Matthias F. Brandl**
Mat. Nr. 0226080
Museumstraße 33/20
6020 Innsbruck

Wien, _____ 2011 _____

Matthias Brandl

Vienna University of Technology

Faculty of Physics

# Diploma Thesis

## Investigation on Chirped Frequency Combs from a Frequency-Shifted Feedback Ti:Sapphire Laser seeded by a Phase-modulated Single-frequency Fiber Laser

**Institute:** Photonics Institute of the UT Vienna

**Supervisors:** Univ.Prof. PhD. Andrius Baltuška
Dr. Oliver D. Mücke

**Author:** Dipl.-Ing. Matthias F. Brandl
Mat. Nr. 0226080
Museumstraße 33/20
6020 Innsbruck

Vienna, _____ 2011 _____

Matthias Brandl

# Abstract

Seeding a frequency-shifted feedback (FSF) laser with a phase-modulated single-frequency laser leads to the generation of an narrow-linewidth chirped frequency comb, which allows to achieve high signal-to-noise ratios of the detected distance-dependent RF beat signal, such that even RF beat signals from diffuse targets can be detected. The seed laser system of this thesis consists of a single frequency DFB laser, an EOM for the phase modulation, and a periodically-poled lithium niobate crystal for second harmonic generation. The FSF laser is a titanium sapphire ring laser with a free spectral range of 77.409MHz. The achieved distance measurement resolution of this system is 6.5$\mu$m. An ultranarrow RF beat of <20Hz was observed which allows further improvement of the length resolution towards the limit of 129nm, set by the <20Hz beat signal.

# Contents

**List of Figures** III

**List of Tables** VI

**1 Introduction** 1

**2 Theoretical background** 3
2.1 Optical frequency-domain ranging with an unseeded FSF laser . . . . . 3
2.2 Seeded FSF Laser . . . . . 6
2.3 Mathematical description of the system . . . . . 9
2.3.1 Definitions . . . . . 9
2.3.2 Michelson interferometer . . . . . 10
2.3.3 Analysis of the phase terms . . . . . 12
2.4 Quasi-phase matching (QPM) . . . . . 13

**3 Experimental setup** 17
3.1 Seed scheme . . . . . 18
3.2 FSF laser . . . . . 21
3.3 Michelson interferometer . . . . . 23

**4 Experimental results** 25
4.1 Optical properties of the FSF laser system . . . . . 25
4.1.1 RF spectrum of the seed light . . . . . 26
4.2 High-reflecting mirror as a target . . . . . 28
4.2.1 Distance measurement . . . . . 28
4.2.2 Dependence on modulation amplitude . . . . . 31
4.2.3 Influence of the optical bandwidth . . . . . 32
4.3 Diffuse target . . . . . 33
4.3.1 Comparison of beat SNR with and without seed . . . . . 33
4.3.2 Finding the optimal seed modulation frequency . . . . . 34
4.3.3 Different distances . . . . . 35
4.3.4 Different targets . . . . . 36
4.4 Measurement with pre-set distance resolution . . . . . 36
4.4.1 RF spectra of the EOM modulation frequency . . . . . 37
4.4.2 Different noise bandwidth . . . . . 38
4.4.3 Detuning the center frequencies . . . . . 40
4.4.4 With Semrock filter . . . . . 41
4.4.5 Diffuse target . . . . . 42

**5 Summary** **44**

**A Appendix** **46**

A.1 Calculation of the beat frequencies . . . . . 46

A.1.1 Michelson interferometer . . . . . 47

A.1.1.1 Autocorrelation terms . . . . . 48

A.1.1.2 Terms with a distance dependence . . . . . 48

A.1.1.3 Substitutions . . . . . 49

A.1.2 Sinusoidal phase modulation . . . . . 50

**Bibliography** **56**

**List of Abbreviations** **59**

**Publications** **60**

**Acknowledgments** **61**

# List of Figures

2.1 Unseeded ring cavity. From [16], p. 6 . . . . . 3

2.2 Michelson interferometer and the resulting RF beat frequency $f_{beat}$ created using the chirped laser light. From [16], p. 3, 4 . . . . . 3

2.3 Frequencies of the chirped frequency combs after the Michelson interferometer [16] p. 11 . . . . . 4

2.4 Zoom of the frequencies and resulting RF beat frequencies at the PD [16] p. 12 . . . . . 4

2.5 Resulting beat frequencies versus distance $L$. From [16], p. 13 . . . . . 5

2.6 Getting rid of the ambiguity by changing the AOM frequency [16] p. 14 . . 6

2.7 Seeded ring cavity . . . . . 6

2.8 Build up of the field of the seeded cavity . . . . . 7

2.9 Frequencies in the cavity with a phase-modulated seed . . . . . 8

2.10 Principle scheme of the measurement setup with a seed laser . . . . . 8

2.11 SHG in a nonlinear crystal for various phase-matching techniques. For QPM, the arrows indicate the poling directions of the ferroelectric domains (white/grey regions). . . . . 15

3.1 Experimental setup of the FSF laser system: the seed generation consists of a single-frequency laser (SFL), which is phase modulated using an EOM and afterwards frequency-doubled in a PPLN waveguide. The seed light passes through a Faraday isolator (FI) and enters the ring cavity of the FSF laser through the zeroth-order input of the AOM. The zeroth-order output of the FSF laser is sent to a Michelson interferometer. The photodiode (PD) at the output of the interferometer detects the distance-dependent RF beat signal. . . . . 17

3.2 Picture of the experimental setup. The free-space-optics of the seed laser setup can be seen in the back of the optical table, the FSF laser in the front on the left side, and the Michelson interferometer in the front on the right side. . . . . 18

3.3 Shows the single-frequency laser, a Koheras Adjustik E15. . . . . 18

3.4 Exhibits the EOM and the PPLN with its temperature controller. . . . . 19

3.5 The free-space-optics part of the seeding setup. With the telescope, the beam diameter of seed light is matched to the beam diameter in the FSF laser. The Faraday isolator prevents light from the FSF laser to reach the PPLN. . . . . 20

3.6 FSF laser near the TiSa crystal. . . . . 22

3.7 FSF laser near the AOM, where one can see the in-coupling of the seed light and the out-coupling of the FSF output. . . . . 22

3.8 Michelson interferometer setup suitable for a diffusely scattering target . . 23

3.9 Setup of the Michelson interferometer for a high-reflector target a) and for a diffusely scattering target b). . . . . 24

4.1 Optical output power in dependence of the pump power . . . . . 26

4.2 Optical spectra of all used configurations of the laser system . . . . . 26

4.3 Measurement of the RF spectrum of the seed light with a modulation frequency of 20MHz and an amplitude of $2V_{pp}$ . . . . . 27

4.4 The panels (a)-(d) show different frequency ranges of the RF spectrum for various seeding conditions. (a) represents the RF spectra from 0-80MHz, where one can see the two distance-dependent peaks and the peak of the FSR. (b) and (c) exhibit the distance-dependent peak with a span of 1MHz and 50kHz. (d) shows the peaks of the FSR with a span of 1MHz and high-resolution zoom to picture the cavity FSR more accurately. . . . . 28

4.5 Scanning of the modulation frequency for distance measurements. The frequency with the highest beat signal corresponds to the distance to measure. 29

4.6 RF spectra for three distances for the seeded and the unseeded case. (a) represents the RF spectra from 0-80MHz, and (b) represents the zooms of the distance-dependent peaks each with a span of 50kHz. Distance 2 corresponds to a distance increase of ≈1cm compared to Distance 1. And for Distance 3, Distance 1 was decreased by ≈100$\mu$m. . . . . 30

4.7 distance-dependent RF beat signal for various modulation voltages (resolution BW 10Hz). . . . . 31

4.8 RF spectra for two different optical spectra of a seeded and an unseeded laser. (a) shows the RF spectra with the pairs of distance-dependent peaks and the FSR peaks. (b) shows the zoom of the distance-dependent peaks. 32

4.9 Scan of the modulation frequency. The achievable distance resolution is reduced due to the reduced optical bandwidth. . . . . 33

4.10 Beat signals for unseeded and seeded cases for a white paper target. Only when the FSF laser is seeded and modulated with the correct modulation frequency, the beat signal can be used for distance measurement, because it has a SNR of 55dB. . . . . 34

4.11 RF spectra for white paper target for various modulation frequencies. . . . 34

4.12 RF beat signals for various modulation frequencies for a white paper target at four different distances. . . . . 35

4.13 EOM modulation driver signals generated with the VSG. Around a center frequency, white noise with a certain bandwidth is added. These spectra are used to modulate the light with the EOM. The center frequency in all figures is 46.705MHz. The $NBW$ is (a) 1kHz, (b) 10kHz, (c) 40kHz, and (d) 100kHz. . . . . 38

4.14 In both panels, the modulation frequency was set to the maximum signal intensity at 47.092kHz. Panel (a) exhibits the RF beat signals where the $NBW$ was smaller than the spectral width of the unseeded case. (b) contains the RF beat signals where the $NBW$ was larger than the spectral width of the unseeded case. . . . . 39

4.15 RF beat signals for various $NBW$s and for two different distances. For Distance 1, the center frequency was 47.092MHz, and for Distance 2 48.640MHz. 39

4.16 In all panels, the modulation frequency was detuned from the maximum signal intensity at 47.092kHz. In panel (a) the NBW was 10kHz, in (b) 40kHz, and in (c) 100kHz. . . . . 40

4.17 A smaller optical bandwidth results in a broader RF beat signal in the unseeded case. The different NBWs shown in this figure are all smaller than the spectral width of the unseeded case. . . . . 42

4.18 RF beat signals for various $NBW$s. When modulating with a larger NBW, one can see how well the different layers of the paper reflect the light. . . . 43

# List of Tables

4.1 SNR and the corresponding modulation frequencies of the beat signal for various targets. . . . . 36

A.1 Pattern for calculating the product of a sum with a sum . . . . . 47

# 1 Introduction

Real-time three-dimensional (3D) video is becoming more and more important. The possibility to control computers or gaming consoles without using a keyboard, mouse, or controller inspires developers to create new kinds of technology. Especially, the gaming industry put a lot of development in distance measurement research to get real-time 3D video devices. But low cost systems, as developed by the gaming industry, are not the only devices of interest. There is also a need for high-accuracy 3D video devices for example in scientific areas. This thesis investigates a concept, with which high-accuracy real-time 3D video could be realized. It will not focus on applying this principle on multiple pixels but on optimizing the measurement process for one single pixel.

There are three fundamental techniques to do distance measurement, namely triangulation, time-of-flight measurements, and interferometry. For the triangulation method [1], there has to be an angle between the light source and the detector. The light source, the detector, and the target are three points of a triangle whose side lengths can be determined with this measurement to recover the unknown distance to the target. Time-of-flight measurement systems have usually a better distance resolution than triangulation system. In time-of-flight systems [2, 3, 4], a light signal is sent from the source to the target and the reflection of this signal is then detected. The time that it takes the light to reach the target and back is measured. By multiplying the time of flight with the speed of light, one can calculate the optical path length travelled by the light signal and, as a result, determine the distance to the target. In comparison with the time-of-flight techniques, a higher distance resolution can be obtained with interferometry, which offers the highest resolution among currently existing methods. In an interferometer, monochromatic light is split at a beam splitter. One part of the light travels a known distance in a reference arm. The rest of the light reaches the target at an unknown distance in the measurement arm and its reflection is brought to interference with the light from the reference arm. From the created heterodyne RF beat signal, one can determine the distance to the target. One requirement for this scheme is that the coherence length of the used light is longer than the length difference of the two arms.

Although there are also other interferometric techniques [5, 6], this thesis focuses only on optical frequency domain ranging (OFDR) with frequency-shifted feedback (FSF) lasers. The theory for FSF lasers had existed for some time, but only in the 1990s they were first built [7, 8, 9] and different operating regimes were found [10, 11, 12]. Nakamura *et al.* demonstrated distance measurements with the OFDR technique employing FSF lasers [13, 14], and they introduced the *Moving Comb Model* [15], that was also discussed in my previous master's thesis [16].

To increase the poor signal-to-noise ratio (SNR) of the principle of Nakamura *et al.*, Yatsenko *et al.* proposed a technique, in which the FSF laser is seeded by a narrow-linewidth seed laser which is phase-modulated [17, 18, 19, 20]. The mathematical model for this type of laser is called *Discrete Frequency Model* and was also introduced by Yatsenko *et al.* [21] as well as a mathematical description of the properties of an FSF laser [22]. These systems show much better SNR. To obtain an even better SNR and to pre-set the distance resolution, one can phase-modulate the seed laser with a frequency range instead of a single frequency, as we have shown in [23].

This thesis is organized as follows: Chapter 2 describes the theoretical background of the measurement process. It covers in detail the *Discrete Frequency Model* to explain why one can detect a distance-dependent beat signal at the detector. Since the *Moving Comb Model* was elaborated on already in my previous master's thesis [16], this thesis only recapitulates the main essence and results of this model, as far as they are a necessary for the understanding of the work presented in this thesis. In the end, the results of both models are compared and, with some restrictions, they match each other perfectly. Also explained in Chapter 2 is the process of optical frequency doubling in a quasi-phasematching crystal which was employed in the seeding scheme.

Chapter 3 presents the laser system for the distance measurement. The main part of the laser system is the titanium-sapphire FSF ring laser. A FSF laser is a laser that contains an acousto-optical modulator (AOM) in the cavity and the cavity is closed via the first-order diffraction of the AOM. This main laser is seeded by a seed laser system, which contains a single-frequency fiber laser, an electro-optical modulator (EOM), and a periodically poled lithium niobate (PPLN) waveguide for second harmonic generation (SHG). The output of the FSF laser enters a Michelson interferometer. One of the arms of the interferometer has a known length and acts as the reference arm. The distance of the other arm is unknown. A photodiode (PD) is placed at the output of the interferometer, where a heterodyne beat signal forms depending on the length difference of the two arms.

In Chapter 4, the distance measurement results are shown. At first, the distance measurement was carried out with a flat mirror as a target. Thereby, the precision was increased from 226$\mu$m without seeding to 6.5$\mu$m with seeding. Subsequently, the mirror target was replaced by a diffuse target. In that case, distance measurement without seeding was no longer possible, but it remaind robust with seeding. Since the distance resolution of this measurement method is so high, the distance resolution for diffuse targets depends mainly on how deeply light penetrates the target before it is reflected or rescattered. At the end of this chapter, the measurement principle with pre-set distance resolution is demonstrated [23]. This might be useful in the development towards a real-time 3D video system based on this OFDR measurement principle.

In the Appendix, the detailed calculations of the beat frequencies obtained from the *Discrete Frequency Model* are presented.

# 2 Theoretical background

## 2.1 Optical frequency-domain ranging with an unseeded FSF laser

This section briefly summarizes the results of the *Moving Comb Model*, described in [15, 16].

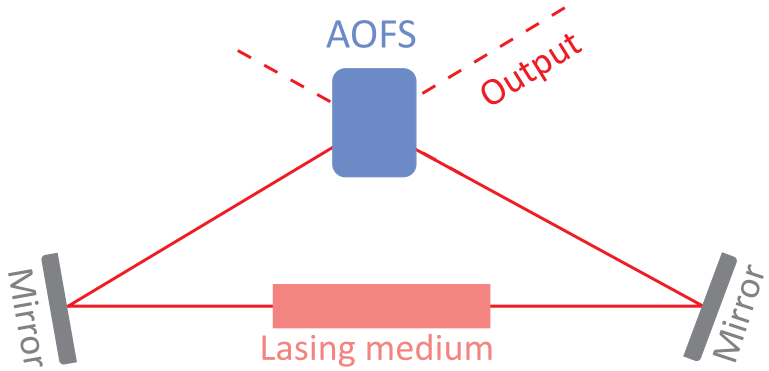


**Figure 2.1.:** Unseeded ring cavity. From [16], p. 6

An unseeded frequency-shifted feedback laser, as shown as a ring cavity in Figure 2.1, creates a chirped frequency comb. In a first approximation, this comb can be described as having a continuous linear chirp. Figure 2.2 shows a setup where such a chirped frequency comb is sent into a Michelson interferometer. The different time delay in the two arms results in a radio-frequency (RF) beat signal $f_{beat}$, which can be seen in this figure, too.

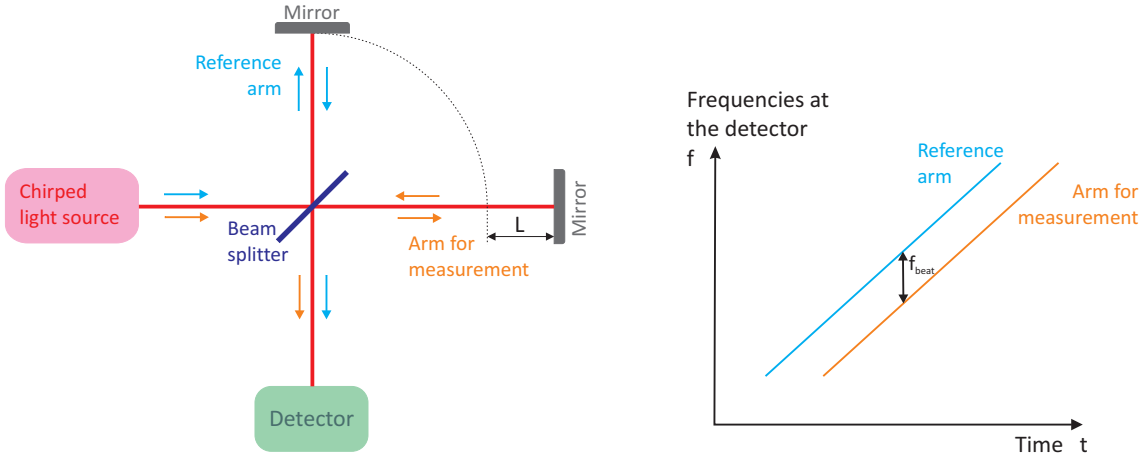


**Figure 2.2.:** Michelson interferometer and the resulting RF beat frequency $f_{beat}$ created using the chirped laser light. From [16], p. 3, 4

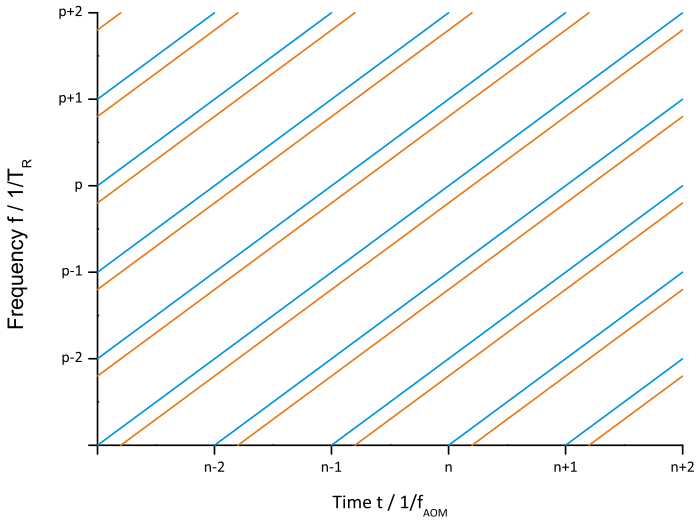


**Figure 2.3.:** Frequencies of the chirped frequency combs after the Michelson interferometer [16] p. 11

In the next step, we will consider many modes. On one side of the spectrum, these modes are amplified from the optical noise and on the other side of the spectrum, they fade out. These modes are separated by a factor of $1/f_{AOM}$ in the time domain and by the cavity free spectral range (FSR) $f_{FSR} = 1/T_R$ in the frequency domain, where $f_{AOM}$ is the AOM frequency and $T_R$ is the round-trip time of the cavity. Figure 2.3 exhibits these frequencies after the Michelson interferometer versus time, and the resulting RF beat frequencies can be seen in Figure 2.4.

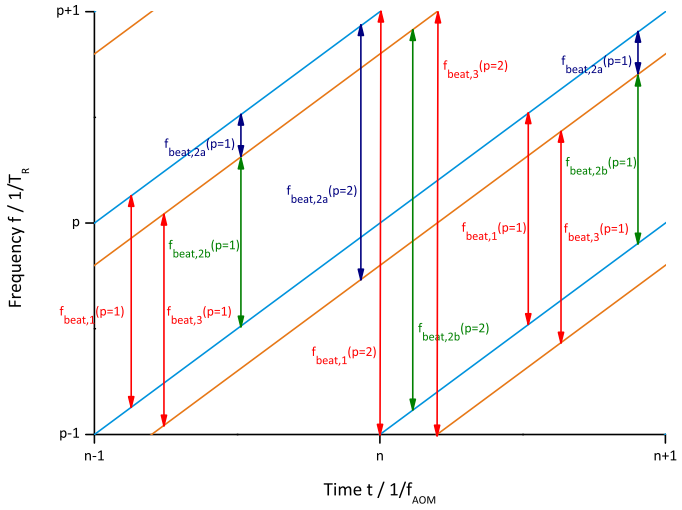


**Figure 2.4.:** Zoom of the frequencies and resulting RF beat frequencies at the PD [16] p. 12

The *Moving Comb Model* of chirped frequencies is a mathematical model for FSF lasers proposed by Nakamura *et al.* [12, 14, 15]. Its results correspond nicely with the measured frequencies, although its ansatz is just a rough approximation. The calculations with this model show some constant beat frequencies that are independent of the distance. These

can be interpreted as autocorrelations of the light in each arm. Their values

$$f_{beat,1}(q,p) = \frac{p}{T_R} \qquad f_{beat,3}(q,p) = \frac{p}{T_R} \tag{2.1}$$

were calculated in Eq. (2.10) and Eq. (2.19) of [16]. In these equations, the integers $q$ and $p$ denote the mode index of the cavity and the beat index, respectively. The terms that exhibit a length dependence are correlations of the light in both arms. The length dependence can be calculated with the following formulas

$$f_{beat,2a}(q,p) = \frac{1}{T_R}\left(p + \frac{L}{L'}\right) \qquad f_{beat,2b}(q,p) = \frac{1}{T_R}\left(p - \frac{L}{L'}\right) \tag{2.2}$$

with

$$L' = \frac{c_0}{2\, f_{AOM}} \tag{2.3}$$

as derived in Eq. (2.13) and Eq. (2.15) of [16], where $L$ is the distance to measure. Since $p$ can be any arbitrary integer, there is a distance ambiguity with an unambiguity range of $L'$. Since one cannot distinguish whether $f_{beat,2a}$ or $f_{beat,2b}$ is measured, the unambiguity range is actually $L'/2$. This ambiguity can easily be seen in Figure 2.5.

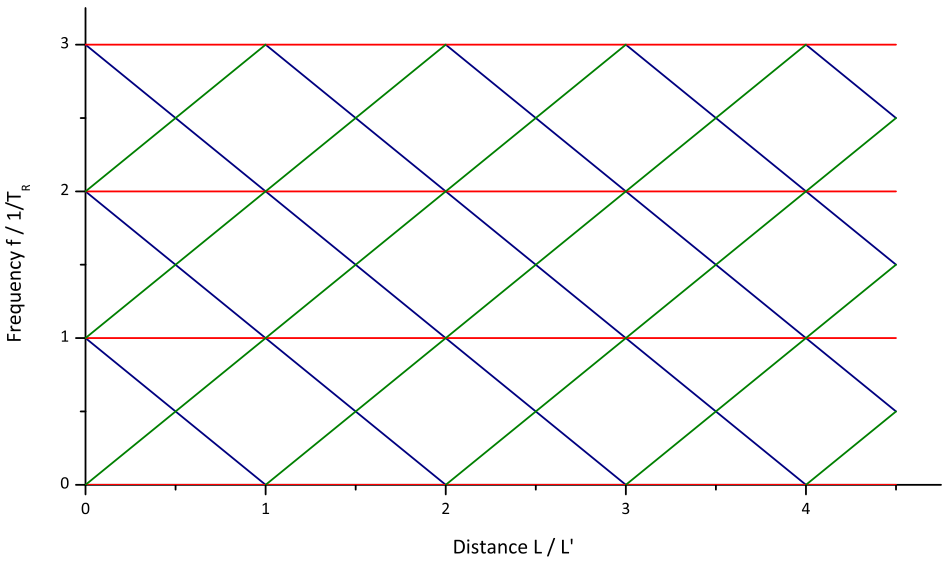


**Figure 2.5.:** Resulting beat frequencies versus distance $L$. From [16], p. 13

One can see why this method is called optical frequency-domain ranging (OFDR) and that there is a frequency ambiguity, too. The unambiguity range in the frequency is $1/(2\,T_R)$. In order to get rid of the ambiguities, the AOM frequency can be changed. Hence, the factor $L'$ will change and one will get another resulting distance and its ambiguities, as can be seen in Figure 2.6. The resulting distances and their ambiguities of both AOM frequencies can then be compared. Only one distance will be an ambiguity in both measurements and that is the actual distance.

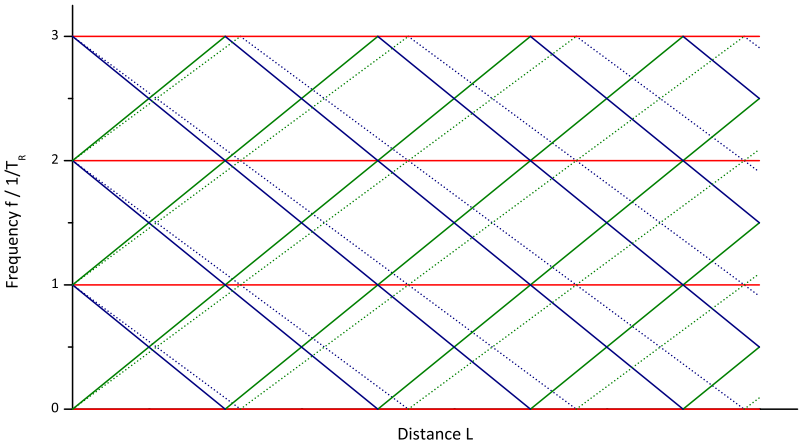


**Figure 2.6.:** Getting rid of the ambiguity by changing the AOM frequency [16] p. 14

## 2.2 Seeded FSF Laser

OFDR with a free-running FSF laser exhibits a low SNR. The SNR is so weak that if one uses a sheet of white paper instead of a mirror in one the arm of the Michelson interferometer, there will not be a distance-dependent signal - there will only be noise. This problem can be overcome with a phase-modulated seed laser, as proposed by Yatsenko *et al.* [21, 17]. The beam of a narrow-linewidth seed laser is directed into the cavity of the FSF laser in a way that the frequency-shifting of the seed starts and the FSF laser is seeded. In order to do that one can use the direction in which one of the two output beams of the unseeded FSF laser exits the cavity through the AOM, as can be seen in Figure 2.7.

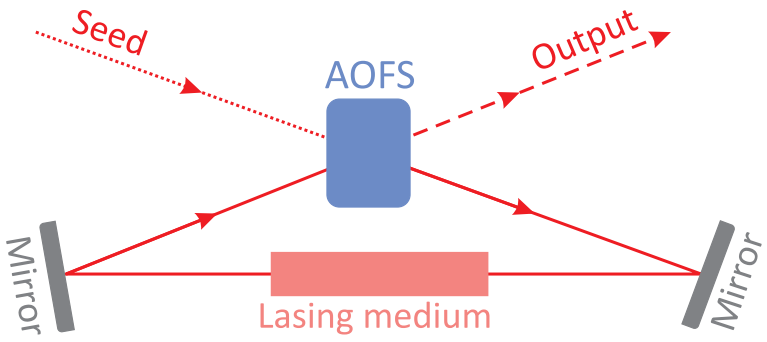


**Figure 2.7.:** Seeded ring cavity

Some of the light of the seed laser is diffracted by the acousto-optic frequency shifter (AOFS) and is directly coupled to the output. **Comment:** This diffracted light is shifted in frequency in the opposite direction as the light in the FSF laser. This means, e.g., if the light in the FSF laser is aligned for frequency up-shift, the diffracted light of the seed will be frequency down-shifted, and vice versa.

The undiffracted light from the seed laser will enter the cavity. The cavity has to be aligned in a way that the FSF output is spectrally close to the narrow line of the seed laser. If the FSF laser is aligned for frequency up-shift, the FSF laser without seed should operate at wavelengths slightly lower (frequencies slightly higher) than that of the seed laser. For frequency down-shift, longer wavelengths (lower frequencies) are required.
If these requirements are fulfilled, the seed will introduce a spectral line that is shifted in frequency after each roundtrip. Hence, a frequency comb forms in the cavity, as can be seen in Figure 2.8.

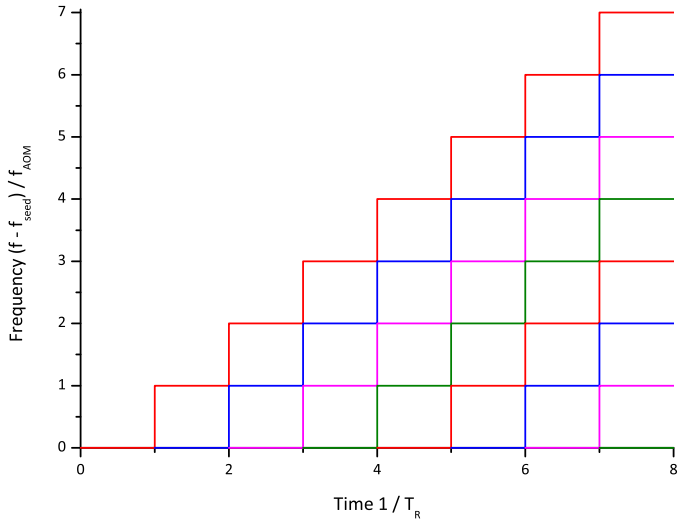


**Figure 2.8.:** Build up of the field of the seeded cavity

If there is no noise present, the only possible RF beat frequencies of this spectrum are $f_{AOM}$ and its harmonics. Since the frequency shift happens once per round-trip, thus every $T_R$, beat frequencies of FSR $f_{FSR} = 1/T_R$ and its harmonics will be present, too. In reality, there will always be additional noise. Whether the SNR increases or decreases with respect to the unseeded case depends only on the product of the electric fields in both arms. For the case of the unseeded FSF laser, one can calculate the product as the unseeded spectral amplitude times itself. For the seeded case, the spectral amplitude of the seed line has to be multiplied with the weak remaining noise. Since the SNR depends on the weak remaining noise, it is not clear if that product leads to an increase or decrease of the SNR.
In order to make sure to increase the SNR, one can perform a phase modulation (PM) of the seed laser with an EOM. The frequencies in the cavity with a PM seed can be seen in Figure 2.9.
If the PM frequency matches one of the two beat frequencies of the distance-dependent beat frequencies, Eq. (2.2), this frequency will have much better SNR. The reason is that the product of the electric field in both arms is now the spectral amplitude of the seed line times the spectral amplitude of the PM side band, which is much larger than the weak noise amplitude. A problem with this measurement scheme arises, because one has to know the beat frequency corresponding to the distance before one does the distance

measurement. This can be solved by sweeping the PM frequency. From the frequency with the best SNR, one can calculate the distance from Eq. (2.2).

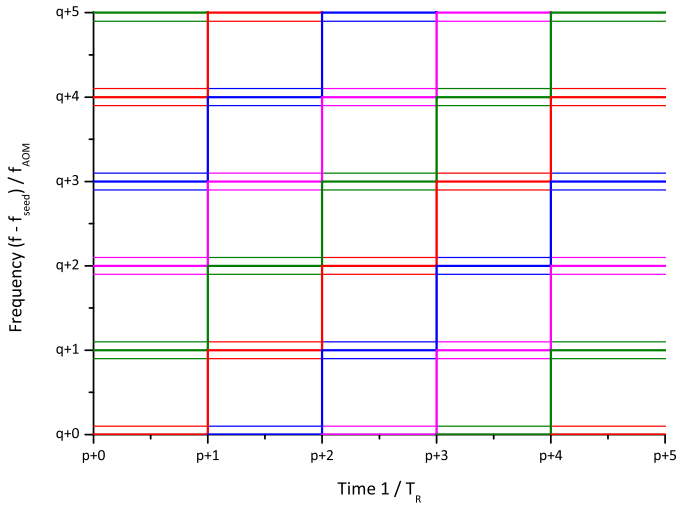


**Figure 2.9.:** Frequencies in the cavity with a phase-modulated seed

A problem for real-time distance measurement is that the individual measurements for the different frequencies have to be done sequently. Hence, one has to wait for each frequency to build up in the cavity before the electrical signal at the detector can be used for measurement. This consumes time which reduces the frame rate of the real time system. Thus, for higher frame rates, it is advisable to use as few frequency comparisons as possible. A higher AOM frequency will decrease the resolvable unambiguity range $L'$ according to Eq.(2.3). Hence, one needs fewer comparisons to reach the same distance resolution. Unfortunately, AOMs with higher modulation frequencies have lower diffraction efficiencies.

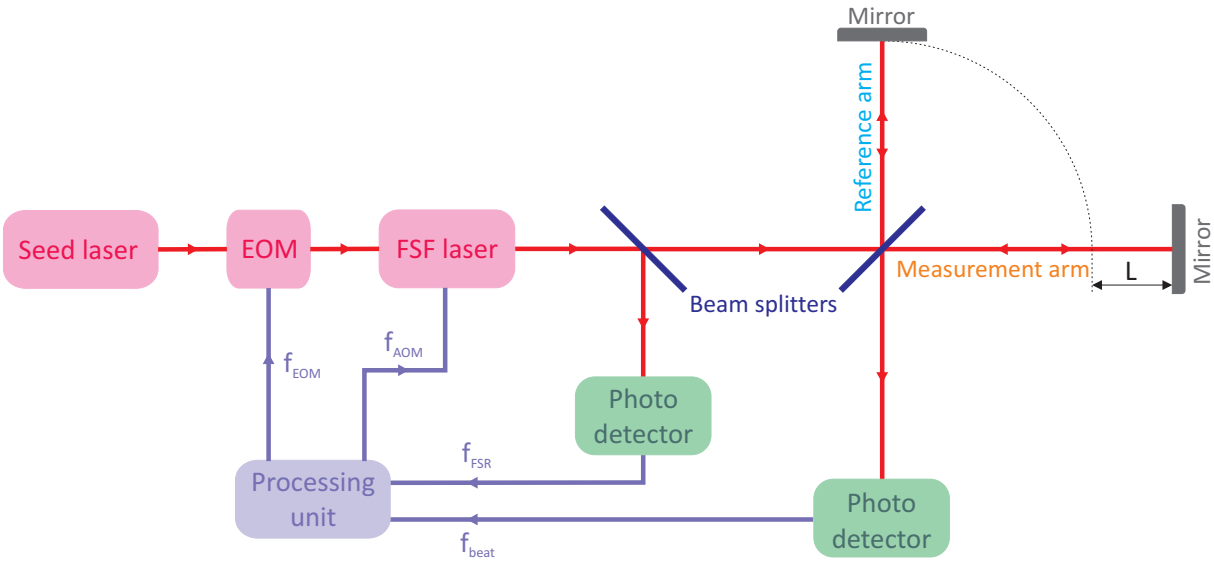


**Figure 2.10.:** Principle scheme of the measurement setup with a seed laser

Figure 2.10 shows a principle scheme of the measurement setup including the seed laser.

The frequencies of the seed laser and the FSF laser have to match each other as described before. The processing unit provides the AOM frequencies ($f_{AOM}$), which can be detuned to get rid of the ambiguity. It also generates the scanning frequencies ($f_{EOM}$). In order to know the exact frequency range for the scanning frequencies, the processing unit receives the FSR of the FSF laser from a photodetector. The autocorrelation of FSF laser light contains the FSR in the RF spectrum. Hence, if a fraction of the output of FSF laser is directed to a photodetector, the measured RF spectrum of the detector signal will show the FSR. The RF spectrum of the output of the Michelson interferometer contains the RF beat $f_{beat}$ with the distance information. The processing unit tests $f_{beat}$ for the frequency $f_{EOM}$. The highest correlation signal of these two frequencies is then the distance to measure, which can be calculated if the frequencies $f_{AOM}$, $f_{FSR}$, and $f_{EOM}$ are known.

## 2.3 Mathematical description of the system

Yatsenko *et al.* introduced the discrete frequency model in [21]. This section presents the calculation of the beat signal frequencies using this model. The details of the calculation can be found in the Appendix A.1.

### 2.3.1 Definitions

The electric field of the FSF laser is defined as

$$E(t) = \sum_{q=0}^{N} E_q(t)\, e^{i\,2\pi\,(f_{seed}\,+\,q\,f_{AOM})\,t} = \sum_{q=0}^{N} \varepsilon_{norm}\; a_q\; e^{i\,2\pi\,((f_{seed}\,+\,q\,f_{AOM})\,t\,+\,\varphi_{seed}(t\,-\,q\,T_R)\,+\,\theta_q)} \tag{2.4}$$

with the complex amplitude

$$E_q(t) = \varepsilon_{norm}\; a_q\; e^{i\,2\pi\,(\varphi_{seed}(t\,-\,q\,T_R)\,+\,\theta_q)} \tag{2.5}$$

where $f_{seed}$ is the (optical) frequency of the seed laser, $f_{AOM}$ is the AOM frequency, $\varphi_{seed}$ is a variable part of the phase, $\theta_q$ is the fixed part of the phase, and $N$ is the number of modes in the cavity. $\varepsilon_{norm}$ stands for a normalization factor and $a_q$ for the amplitude of the mode $q$. This together forms a frequency comb starting at the frequency $f_{seed}$. The comb lines are separated by $f_{AOM}$ and there are $N + 1$ lines.
As an ansatz for the constant phase of each mode, we use

$$\theta_q = T_R\, q \left( f_{seed} + (q+1)\;\frac{f_{AOM}}{2} \right) + \theta_0 \tag{2.6}$$

where $\theta_0$ is a constant phase shift and the other terms correspond to the phase shift caused by the propagation in the FSF laser.
The intensity is defined as

$$I\,(t) = \frac{n c_0 \epsilon_0}{2}\,|E\,(t)|^2 \quad . \tag{2.7}$$

### 2.3.2 Michelson interferometer

The intensity after the Michelson interferometer can be obtained as follows

$$I(t) \propto \left|\delta\, E(t) + \eta\, E\left(t - \frac{2L}{c_0}\right)\, e^{i\,2\pi\,\Delta\phi}\right|^2 = \delta^2\,|E(t)|^2 + \eta^2\,\left|E\left(t - \frac{2L}{c_0}\right)\right|^2 + \delta\eta\,\left|E^*(t)\;\; E\left(t - \frac{2L}{c_0}\right)\, e^{i\,2\pi\,\Delta\phi} + E(t)\;\; E^*\left(t - \frac{2L}{c_0}\right)\, e^{-i\,2\pi\,\Delta\phi}\right| \tag{2.8}$$

$$I(t) \propto I_1(t) + I_2(t) + I_3(t) \tag{2.9}$$

$$I_1(t) = \delta^2\,|E(t)|^2 \tag{2.10}$$

$$I_2(t) = \eta^2\,\left|E\left(t - \frac{2L}{c_0}\right)\right|^2 \tag{2.11}$$

$$I_3(t) = \delta\eta\,\left|E^*(t)\;\; E\left(t - \frac{2L}{c_0}\right)\, e^{i\,2\pi\,\Delta\phi} + E(t)\;\; E^*\left(t - \frac{2L}{c_0}\right)\, e^{-i\,2\pi\,\Delta\phi}\right| \tag{2.12}$$

$\delta$ and $\eta$ represent the dampings in the two arms, and $\Delta\phi$ represents the difference in the phase shift at the two targets due to different target materials. The intensity can be split in three terms. $I_1(t)$ and $I_2(t)$ correspond to autocorrelations of the light from the individual arms. $I_3(t)$ is a correlation term of the two arms and it will yield the distance dependence.

As discussed earlier, we want to perform phase modulation of the seed laser with an EOM. Hence,

$$\varphi_{seed}(t) = \varphi_0 + A_{EOM}\;\sin\left(2\pi\, f_{EOM}\, t\right) \tag{2.13}$$

where $\varphi_0$ is a constant phase offset due to the EOM crystal. The second term represents a phase modulation with a sine of frequency $f_{EOM}$ and amplitude $A_{EOM}$.

In order to obtain the final results, we define the beat index $p$ and use the Bessel functions $J_n$. $p$ indicates with which neighbor the interference term has to be calculated, e.g., $p = 0$ means that the mode $q$ only interferes with light of mode $q$ (of the same or the other arm). $n$ is the index for the Bessel functions. The final results are shown in the following

$$I_1(t) = \delta^2 \sum_{p=0}^{N} \sum_{q=0}^{N-p} \sum_{n=-\infty}^{\infty} (-1)^n\,|\varepsilon_{norm}|^2\, a_q\, a_{q+p}\,\left(J_{2n}(M_1)\cos\left(2\pi\left(f_{even}\, t + \varphi_{1,even}\right)\right)\right. + \left. J_{2n-1}(M_1)\sin\left(2\pi\left(f_{odd}\, t + \varphi_{1,odd}\right)\right)\right) \tag{2.14}$$

$$I_2(t) = \eta^2 \sum_{p=0}^{N} \sum_{q=0}^{N-p} \sum_{n=-\infty}^{\infty} (-1)^n\,|\varepsilon_{norm}|^2\, a_q\, a_{q+p}\,\left(J_{2n}(M_1)\cos\left(2\pi\left(f_{even}\, t + \varphi_{2,even}\right)\right)\right. + \left. J_{2n-1}(M_1)\sin\left(2\pi\left(f_{odd}\, t + \varphi_{2,odd}\right)\right)\right) \tag{2.15}$$

$$I_3(t) = \delta\eta \sum_{p=0}^{N} \sum_{q=0}^{N-p} \sum_{n=-\infty}^{\infty} (-1)^n\,|\varepsilon_{norm}|^2\, a_q\, a_{q+p}\,\left(J_{2n}(M_{3a})\cos\left(2\pi\left(f_{even}\, t + \varphi_{3a,even}\right)\right)\right. + J_{2n-1}(M_{3a})\sin\left(2\pi\left(f_{odd}\, t + \varphi_{3a,odd}\right)\right) + J_{2n}(M_{3b})\cos\left(2\pi\left(f_{even}\, t + \varphi_{3b,even}\right)\right) + \left. J_{2n-1}(M_{3b})\sin\left(2\pi\left(f_{odd}\, t + \varphi_{3b,odd}\right)\right)\right) \tag{2.16}$$

where

$$M_1 = 4\pi\, A_{EOM} \sin\left(\pi\, p\, f_{EOM} T_R\right) \tag{2.17}$$

$$M_{3a} = 4\pi\, A_{EOM} \sin\left(2\pi\, f_{EOM}\, \left(\frac{L}{c_0} + \frac{p}{2} T_R\right)\right) \tag{2.18}$$

$$M_{3b} = 4\pi\, A_{EOM} \sin\left(2\pi\, f_{EOM}\, \left(-\frac{L}{c_0} + \frac{p}{2} T_R\right)\right) \tag{2.19}$$

$$f_{odd} = p\, f_{AOM} + (2n-1)\, f_{EOM} \tag{2.20}$$

$$f_{even} = p\, f_{AOM} + 2n f_{EOM} \tag{2.21}$$

and the phase terms

$$\varphi_{1,odd} = T_R \left( p\, f_{seed} + \left(p^2 + p + 2qp\right)\, \frac{f_{AOM}}{2} - (2n-1)\left(q + \frac{p}{2}\right) f_{EOM} \right) \tag{2.22}$$

$$\varphi_{1,even} = T_R \left( p\, f_{seed} + \left(p^2 + p + 2qp\right)\, \frac{f_{AOM}}{2} - n\,(2q+p)\, f_{EOM} \right) \tag{2.23}$$

$$\begin{aligned} \varphi_{2,odd} = {} & T_R \left( p\, f_{seed} + \left(p^2 + p + 2qp\right)\, \frac{f_{AOM}}{2} - (2n-1)\left(q + \frac{p}{2}\right) f_{EOM} \right) \\ & - \left(p\, f_{AOM} + (2n-1)\, f_{EOM}\right) \frac{2L}{c_0} \end{aligned} \tag{2.24}$$

$$\begin{aligned} \varphi_{2,even} = {} & T_R \left( p\, f_{seed} + \left(p^2 + p + 2qp\right)\, \frac{f_{AOM}}{2} - n\,(2q+p)\, f_{EOM} \right) \\ & - \left(p\, f_{AOM} + 2n f_{EOM}\right) \frac{2L}{c_0} \end{aligned} \tag{2.25}$$

$$\begin{aligned} \varphi_{3a,odd} = {} & T_R \left( p\, f_{seed} + \left(p^2 + p + 2qp\right)\, \frac{f_{AOM}}{2} - (2n-1)\left(q + \frac{p}{2}\right) f_{EOM} \right) \\ & - \left( f_{seed} + (q+p)\, f_{AOM} + \frac{2n-1}{2}\, f_{EOM} \right) \frac{2L}{c_0} + \Delta\phi \end{aligned} \tag{2.26}$$

$$\begin{aligned} \varphi_{3a,even} = {} & T_R \left( p\, f_{seed} + \left(p^2 + p + 2qp\right)\, \frac{f_{AOM}}{2} - n\,(2q+p)\, f_{EOM} \right) \\ & - \left( f_{seed} + (q+p)\, f_{AOM} + \frac{2n-1}{2}\, f_{EOM} \right) \frac{2L}{c_0} + \Delta\phi \end{aligned} \tag{2.27}$$

$$\begin{aligned} \varphi_{3b,odd} = {} & T_R \left( p\, f_{seed} + \left(p^2 + p + 2qp\right)\, \frac{f_{AOM}}{2} - (2n-1)\left(q + \frac{p}{2}\right) f_{EOM} \right) \\ & + \left( f_{seed} + (q+p)\, f_{AOM} + \frac{2n-1}{2}\, f_{EOM} \right) \frac{2L}{c_0} - \Delta\phi \end{aligned} \tag{2.28}$$

$$\begin{aligned} \varphi_{3b,even} = {} & T_R \left( p\, f_{seed} + \left(p^2 + p + 2qp\right)\, \frac{f_{AOM}}{2} - n\,(2q+p)\, f_{EOM} \right) \\ & + \left( f_{seed} + (q+p)\, f_{AOM} + n\, f_{EOM} \right) \frac{2L}{c_0} - \Delta\phi \end{aligned} \tag{2.29}$$

### 2.3.3 Analysis of the phase terms

In this section, we want to examine the phase terms. We are interested in having the $f_{EOM}$ matched to the distance $L$. And, we will restrict ourselves to only the odd terms with $p = 0$ and $n = 1$ and we will neglect the other terms. $p = 0$ and $n = 1$ means that we only consider beat signals from the first side peaks, the first sidebands of the phase modulation, with the main peak. Hence,

$$f_{odd} = f_{EOM} \tag{2.30}$$

$$\varphi_{1,odd} = -q\, T_R\, f_{EOM} \tag{2.31}$$

$$\varphi_{2,odd} = -q\, T_R\, f_{EOM} - f_{EOM}\, \frac{2L}{c_0} \tag{2.32}$$

$$\varphi_{3a,odd} = -q\, T_R\, f_{EOM} - \left( f_{seed} + q\, f_{AOM} + \frac{1}{2}\, f_{EOM} \right) \frac{2L}{c_0} + \Delta\phi \tag{2.33}$$

$$\varphi_{3b,odd} = -q\, T_R\, f_{EOM} + \left( f_{seed} + q\, f_{AOM} + \frac{1}{2}\, f_{EOM} \right) \frac{2L}{c_0} - \Delta\phi \tag{2.34}$$

In order to get a good SNR, the modes have to be in phase. Hence, $\varphi\,(q) - \varphi\,(q+1)$ has to be an integer value.

$$\varphi_{1,odd}\,(q) - \varphi_{1,odd}\,(q+1) = T_R\, f_{EOM} = \lambda_1 \tag{2.35}$$

$$\varphi_{2,odd}\,(q) - \varphi_{3,odd}\,(q+1) = T_R\, f_{EOM} = \lambda_1 \tag{2.36}$$

$$\varphi_{3a,odd}\,(q) - \varphi_{2a,odd}\,(q+1) = T_R\, f_{EOM} - f_{AOM}\, \frac{2L}{c_0} = \lambda_2 \tag{2.37}$$

$$\varphi_{3b,odd}\,(q) - \varphi_{2b,odd}\,(q+1) = T_R\, f_{EOM} + f_{AOM}\, \frac{2L}{c_0} = \lambda_3 \tag{2.38}$$

where $\lambda_1$, $\lambda_2$, and $\lambda_3$ are integer values. To get a good SNR from the autocorrelation terms $I_1$, and $I_3$, we have to use a multiple of the FSR as the EOM frequency. These terms show no distance dependence, and they match the results from the moving comb model, Eq. (2.1).

$$f_{EOM,auto} = \frac{\lambda_1}{T_R} \tag{2.39}$$

The distance-dependent terms match the ones obtained from the moving comb model nicely, Eq. (2.2).

$$f_{EOM,dist1} = \frac{1}{T_R} \left( \lambda_2 + \frac{2 f_{AOM}}{c_0}\, L \right) = \frac{1}{T_R} \left( \lambda_2 + \frac{L}{L'} \right) \tag{2.40}$$

$$f_{EOM,dist2} = \frac{1}{T_R} \left( \lambda_3 - \frac{2 f_{AOM}}{c_0}\, L \right) = \frac{1}{T_R} \left( \lambda_3 - \frac{L}{L'} \right) \tag{2.41}$$

where $L' = \frac{c_0}{2 f_{AOM}}$, as defined in Eq. (2.3). Since noise is always present, the frequencies $f_{EOM,auto}$, $f_{EOM,dist1}$, and $f_{EOM,dist2}$, as well as $f_{EOM}$, will always appear in the RF spectrum, even if $f_{EOM}$ does not match one of the other frequencies. But if $f_{EOM}$ matches one of the other frequencies, the SNR of this frequency will increase significantly.

## 2.4 Quasi-phase matching (QPM)

In Chapter 3, the laser system will be discussed and it contains a PPLN crystal for SHG. The problem with SHG in any nonlinear crystal is that the relative phase between the interacting waves has to stay constant during propagation to obtain high conversion efficiencies. However, due to dispersion, the relative phase will in general not remain constant. The most common phase-matching technique is using birefringence crystal to match the phase velocities of the two waves with the extraordinary and the ordinary rays in the crystal. Another technique to achieve efficient SHG employs quasi-phase matching (QPM) [24, 25]. Here, the phase velocities of the two waves are not matched. But a periodic modulation of the properties of the nonlinear medium corrects the relative phase at regular intervals. PPLN crystals are based on the concept of QPM. Lithium-niobate is a ferroelectric material. The direction of the ferroelectricity is reversed at regular intervals along the direction of propagation, as shown in Figure 2.11, resulting in the so-called periodic poling. This section will briefly lay out the concept of QPM along the lines of [24, 25].

The incoming (fundamental) wave has an amplitude of $E_1$ with a frequency $\omega_1$. With that and the corresponding refractive index $n_1$, the wave vector $k_1 = \frac{n_1\omega_1}{c_0}$ can be calculated. Similarly, the amplitude $E_2$, the frequency $\omega_2$, and the refractive index $n_2$ of the created (second-harmonic) wave can be defined, and its wave vector $k_2 = \frac{n_2\omega_2}{c_0}$ can be derived. This wave is created in a material with quadratic nonlinear susceptibility $d$. Thus, the created wave is proportional to $d\,E_1^2$ and has a frequency $\omega_2 = 2\omega_1$ and a wave vector $2k_1$. The conversion of the SHG is defined via the intensity. Therefore, it is proportional to $E_2^2$. The coherence length is defined as the length, where the relative phase between the fundamental and second-harmonic (SH) changes by a factor of $\pi$, i.e,

$$l_{coh} = \frac{\pi}{k_2 - 2k_1} = \frac{\lambda}{4\,(n_2 - n_1)} \tag{2.42}$$

where $\lambda$ is the vacuum wavelength of the fundamental.

Let us now consider the simple case, where the fundamental wave is a constant plane wave propagating in the z-direction. The evolution of the second harmonic field is thus

$$\frac{dE_2}{dz} = i\,\frac{\omega_1 E_1^2}{n_2 c_0}\,d(z)\,e^{-i(k_2-2k_1)z} = \Gamma\,d(z)\,e^{-i\,\Delta k'\,z} \tag{2.43}$$

$$\text{with} \qquad \Gamma = i\,\frac{\omega_1 E_1^2}{n_2 c_0} \tag{2.44}$$

$$\text{and} \qquad \Delta k' = k_2 - 2k_1 = \frac{\pi}{l_{coh}} \quad . \tag{2.45}$$

$d(z)$ represents the spatially varying nonlinear SHG coefficient, and $\Delta k'$ the wave vector mismatch. One can easily obtain $E_2$ by integrating, hence

$$E_2(L) = \Gamma \int_0^L d(z)\,e^{-i\,\Delta k'\,z}\,dz \tag{2.46}$$

where $L$ is the length of the crystal or any length within the crystal. One can see that the generated electric field is proportional to the Fourier transform of the SHG coefficient.

For perfect conventional phase matching (in birefringent crystals), the SHG coefficient is a constant ($d(z) = d_{eff}$) and the wave vector mismatch vanishes ($\Delta k' = 0$). Hence,

$$E_2(L) = \Gamma \, d_{eff} \, L \qquad . \tag{2.47}$$

For QPM, one can analyze the Fourier transform of $d(z)$. At first, the SHG coefficient is normalized, like

$$g(z) = \frac{d(z)}{d_{eff}} \tag{2.48}$$

and its Fourier transform follows as

$$G\left(\Delta k'\right) = \frac{1}{L} \int_0^L g(z) \, e^{-i \, \Delta k' \, z} \, dz \tag{2.49}$$

Eq. (2.46) can now be written as

$$E_2(L) = \Gamma \, d_{eff} \, L \; G\left(\Delta k'\right) \quad . \tag{2.50}$$

This equation is remarkably similar to Eq. (2.47). Due to the normalization, the absolute value of Eq. (2.49) is smaller than 1. $G\left(\Delta k'\right)$ represents the term that states how well QPM matches perfect conventional phase matching. Therefore, one can refer to $G\left(\Delta k'\right)$ as the mismatch function, which transforms the normalized SHG coefficient to the mismatch domain.

The normalized SHG coefficient $g(z)$ is a periodic function for QPM, and is defined as

$$g(z) = \sum_{m=-\infty}^{\infty} G_m \, e^{i \, K_m \, z} \tag{2.51}$$

with the wave vectors

$$K_m = \frac{2 \, \pi \, m}{\Lambda} \qquad . \tag{2.52}$$

When inserting these equations in Eq. (2.49), $\Delta k'$ and $K_m$ add up to the total wave-vector mismatch $\Delta k = \Delta k' - K_m$. For phase matching, $K_m$ is roughly $\Delta k'$. Therefore, $G\left(\Delta k'\right)$ and $E_2$ are dominated by the $m$-th term.

$$E_2 = \Gamma \, d_{eff} \, L \, G_m \, e^{-i \, \frac{\Delta k \, L}{2}} \, \operatorname{sinc}\left(\frac{\Delta k \, L}{2}\right) \tag{2.53}$$

For perfect phase matching, the total wave-vector mismatch vanishes, and

$$E_2 = \Gamma \, d_{eff} \, L \, G_m \tag{2.54}$$

which is the same as Eq. (2.47) except for the mismatch term $G_m$.

In PPLN crystals, the ferroelectric domains are periodically reversed. Thus, the normalized SHG coefficient $g(z)$ can be defined as a rectangular function with the values $\pm 1$ and the period $\Lambda$. The duty cycle is $D = l/\Lambda$, where $l$ is the length of the first ferroelectric domain during one period, and the corresponding Fourier coefficient is

$$G_m = \frac{2}{\pi\, m} \sin(\pi\, m\, D) \quad . \tag{2.55}$$

The optimum duty cycle is 0.5 for odd numbers and 0.25 for even numbers. The highest efficiency can be found for $m = 1$. Thus,

$$E_2 = \Gamma\, d_{eff}\, L\, \frac{2}{\pi} \quad . \tag{2.56}$$

Thus, the absolute value of the conversion is reduced by a factor of $\left(\frac{2}{\pi}\right)^2$ compared to perfect phase matching in birefringent crystals.

If one wants to be more accurate and include the next higher Fourier coefficient, the $m = 3$ term has to be considered as well. Then,

$$E_2 = \Gamma\, d_{eff}\, L\, \frac{2}{\pi} \left(1 + \frac{1}{3}\, e^{i\, \frac{2\pi}{\Lambda} L}\, \mathrm{sinc}\left(\frac{2\,\pi}{\Lambda}\, L\right)\right) \quad . \tag{2.57}$$

The conversion efficiency along the propagation axis can be seen in the following figure.

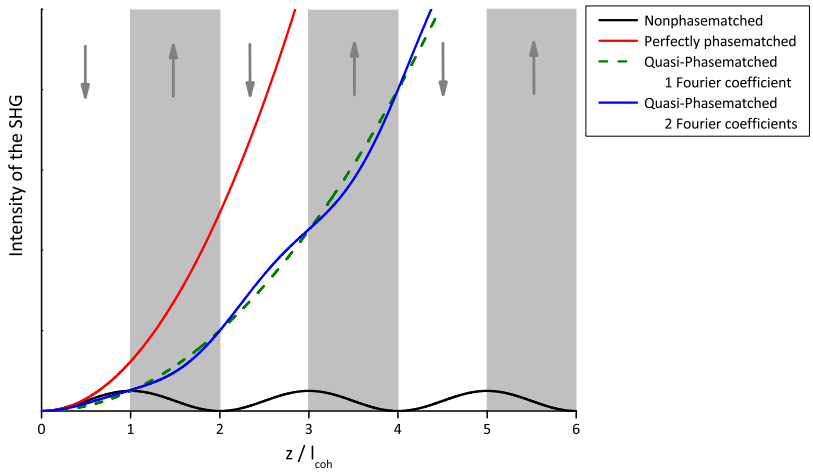


**Figure 2.11.:** SHG in a nonlinear crystal for various phase-matching techniques. For QPM, the arrows indicate the poling directions of the ferroelectric domains (white/grey regions).

Phase matching in birefringent crystals allows harmonic generation with high conversion efficiencies. QPM offers a possibility to influence the phase matching of the wave vectors through an engineerable parameter, the periodical reversal of the ferroelectricity. In crystals with QPM, the polarization of the light does not necessarily have to change for the higher harmonic. For some materials like lithium-niobate, the nonlinear coefficient $d_{eff}$ is much higher for polarization maintaining interactions than for polarization changing

interactions. This allows higher conversion efficiencies with QPM than with conventional phase matching despite the efficiency being a factor of $\left(\frac{2}{\pi}\right)^2$ lower than in the case of ideal phase matching. Hence, QPM is widely used with lower light intensities, as for frequency-doubling continuous-wave light in this thesis. Another advantage of QPM is that one can avoid spatial walk-off which limits the conversion efficiency in long, birefringent crystals. In QPM, one can use a crystal axis as the propagation direction and thereby avoid the spatial walk-off.

# 3 Experimental setup

As part of my master's thesis work in electrical engineering [16], I built an *unseeded* FSF titanium sapphire (TiSa) ring laser. In the present diploma thesis work in technical physics, this laser system was extended by adding phase-modulated ultranarrow-linewidth single-frequency seeding of this FSF laser. This chapter will focus on the upgraded setup of this seeded FSF laser system.

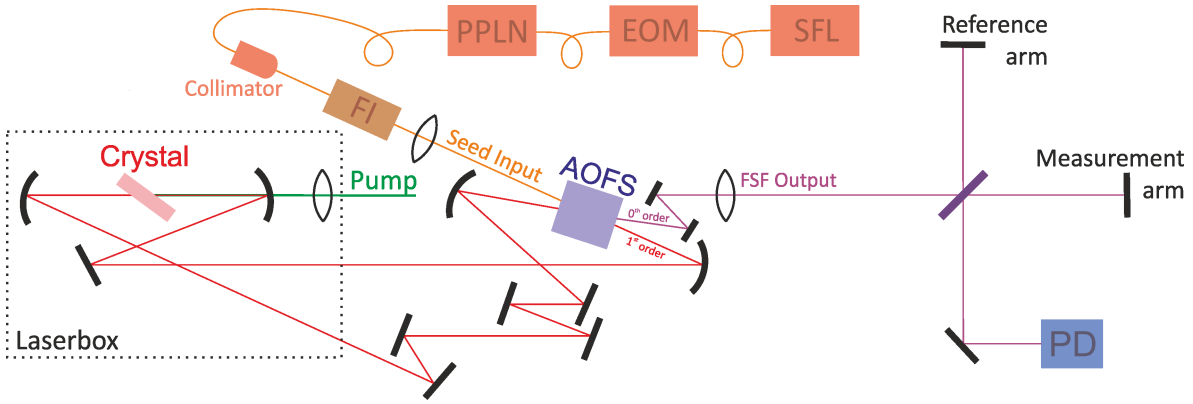


**Figure 3.1.:** Experimental setup of the FSF laser system: the seed generation consists of a single-frequency laser (SFL), which is phase modulated using an EOM and afterwards frequency-doubled in a PPLN waveguide. The seed light passes through a Faraday isolator (FI) and enters the ring cavity of the FSF laser through the zeroth-order input of the AOM. The zeroth-order output of the FSF laser is sent to a Michelson interferometer. The photodiode (PD) at the output of the interferometer detects the distance-dependent RF beat signal.

The laser system can be seen in Figure 3.1. The system can be divided into three major parts. The first part is the seed laser, which contains the orange and light brown components depicted in Figure 3.1. The second part is the FSF laser itself, which is drawn in red. And the third part consists of the Michelson interferometer and the photodetector plotted in purple. The following sections will focus on each part individually. The following figure shows a photo of the whole laser setup in the lab.

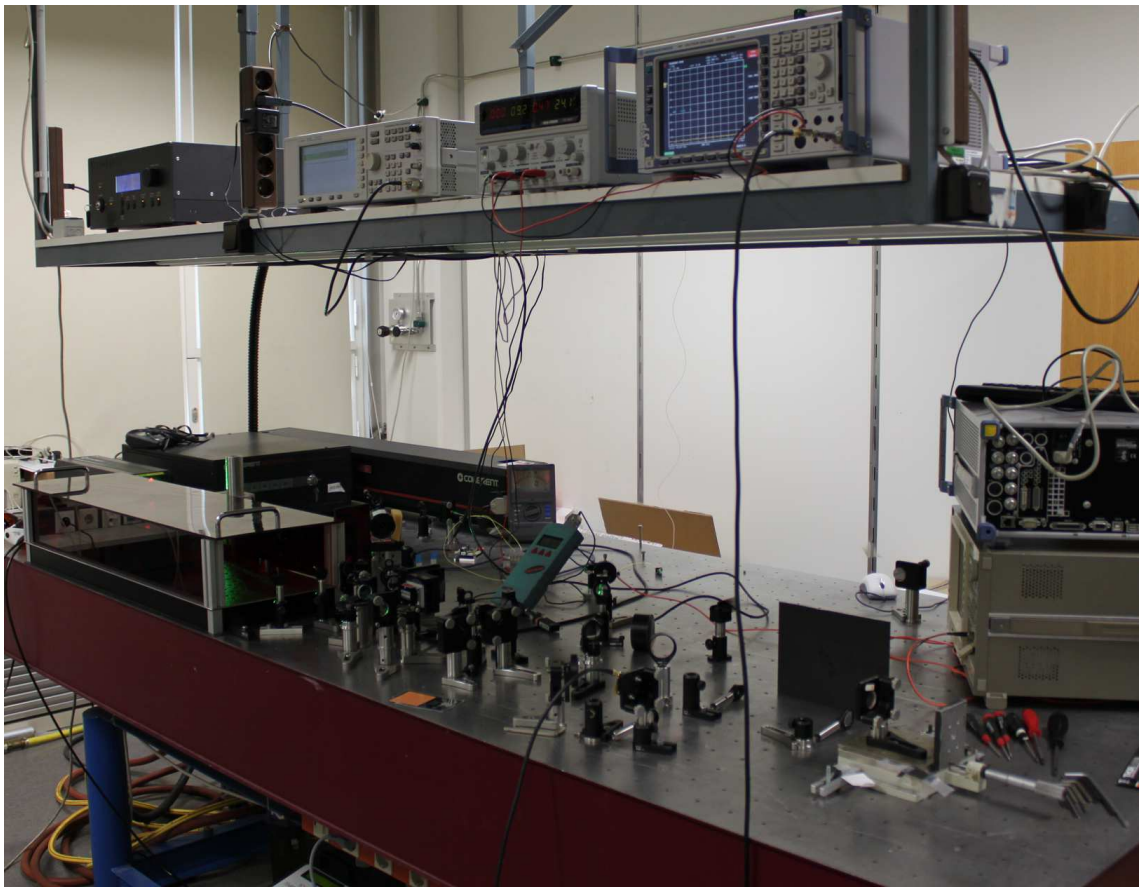

**Figure 3.2.:** Picture of the experimental setup. The free-space-optics of the seed laser setup can be seen in the back of the optical table, the FSF laser in the front on the left side, and the Michelson interferometer in the front on the right side.

## 3.1 Seed scheme


**Figure 3.3.:** Shows the single-frequency laser, a Koheras Adjustik E15.

As seen in Figure 3.1, the seed generation consists of a single-frequency laser (SFL), an EOM, and a PPLN waveguide for SHG. One could, of course, just use a SFL directly at the desired wavelength and buy a matching EOM. This would save the money for the PPLN. The idea behind the chosen scheme was that after a first proof-of-principle experiment, the FSF laser will later be rebuilt as an Erbium-doped fiber laser at approximately twice the wavelength. In this case, one would have to buy a new expensive seed laser and a new EOM for the new wavelength. And since the detection has to be done with silicon

photodiodes, one would have to buy a PPLN, too, to work with, and especially detect, wavelengths shorter than 1$\mu$m.
The decision was made to purchase a SFL at 1555nm to save money by only buying one SFL and one EOM. Another reason for choosing the SFL and the EOM for 1555nm was that this wavelength is in telecommunication C-band. There, all kinds of components are available at moderate prices, including the SFL, the EOM, and PPLN waveguides for SHG. All these components are pigtailed, which is particularly important for the EOM. Waveguides have very small dimensions perpendicular to the direction of propagation, and the electro-optic effect in an EOM is proportional to the electric field. Hence, one can achieve the same electric field with smaller dimensions at lower voltages than with bigger dimensions. The voltage that creates a relative phase shift of $\pi$, $U_\pi$, is in the order of several volts for waveguides compared to several hundred volts for big crystals. That makes the modulation easier to establish and the modulation faster, because one does not have to work with hundreds of volts.

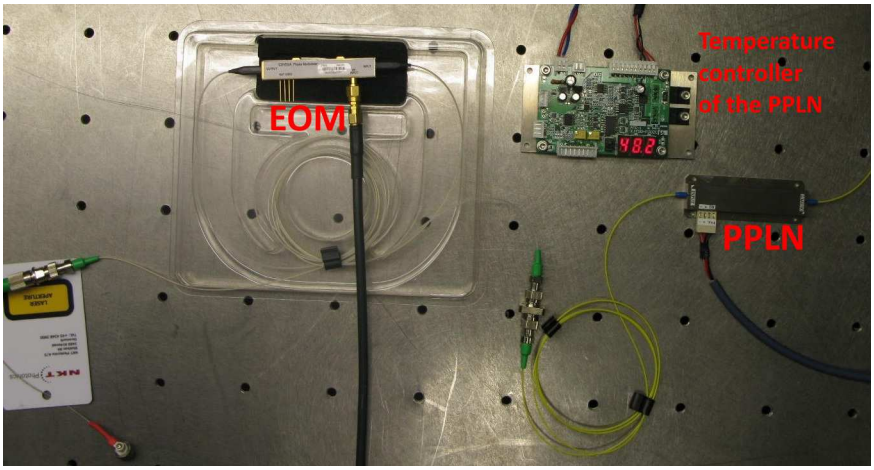


**Figure 3.4.:** Exhibits the EOM and the PPLN with its temperature controller.

The main components that were used for the seed generation are

- **Koheras Adjustik E15** from *NKT Photonics*: this is the SFL with a linewidth smaller than 1kHz on a time scale of 120$\mu$s. It is a distributed feedback (DFB) fiber laser with a maximum output of 125mW. It has a polarization-maintaining output with an FC/APC connector.

- **LN53-10PAASTL** from *Thorlabs Quantum Electronics* (*Covega*): it is a lithium niobate EOM with a maximum modulation frequency of 10GHz and a typical $U_\pi$ of 3.5V.

- **Periodically poled MgO-doped lithium niobate waveguide** from *HC Photonics*: this is the PPLN for frequency-doubling from 1555nm to 777.5nm. The temperature range extends from 30° to 60°C and the conversion efficiency was specified to be greater than 60% per Watt and per cm$^2$.

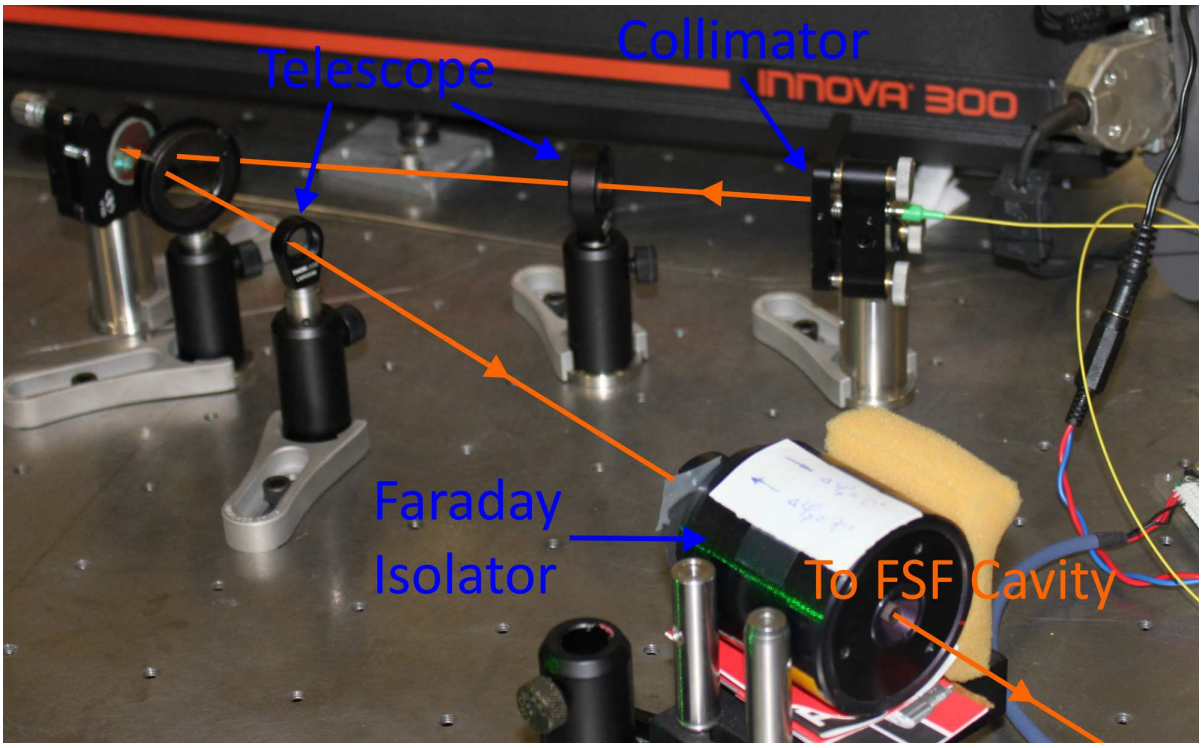


**Figure 3.5.:** The free-space-optics part of the seeding setup. With the telescope, the beam diameter of seed light is matched to the beam diameter in the FSF laser. The Faraday isolator prevents light from the FSF laser to reach the PPLN.

The optical setup of the fiber part (SFL, EOM, and PPLN) of the seed setup was very simple, because one only had to connect the FC/APC connectors and switch on the Adjustik and the temperature controller of the PPLN. The light exiting the fiber after the PPLN was collimated using a fiber collimator. Unfortunately, the beam diameter of the seed light did not match the beam diameter of the FSF laser, which is a requirement for good seeding. Hence, the beam diameter of the seed was increased using a telescope, as can be seen in Figure 3.5. After the telescope the light passed through a Faraday isolator which protects the PPLN from possible high light intensities coming from the FSF laser. The maximum seed light power was 2.7mW after the fiber collimator, which was sufficient for seeding.

## 3.2 FSF laser

In the previous chapter, seed laser system was discussed. And in this chapter, the FSF laser which is the laser that needs to be seeded will be shown. Figure 2.1 exhibits a principle setup of an FSF laser. As already mentioned, the laser used during this thesis was a TiSa ring laser. Inside the cavity, there is an AOM and the cavity is closed via the first order diffraction. Thereby, the light in the cavity undergoes a frequency-shift of the AOM frequency each round-trip.
In the laser setup of my previous thesis, there was a Faraday isolator in the cavity, too, to make the laser lase only in one direction of the ring cavity. But due to asymmetries, one direction will very likely be favored over the other. Hence, the Faraday isolator can be removed from the cavity, causing less loss. And by tilting the AOM, the direction of the lasing can be chosen. It can happen that while optimizing the laser, the direction of lasing changes. Therefore, the Faraday isolator was put between the seed laser system and the FSF laser to only let light pass from the seed to the FSF laser and not the other way round. The optical path length of this FSF laser was 3.873m.
The seed laser has to match the mode size, and the seed light in the FSF cavity has to point in the exact same direction as the FSF laser light. The mode matching is done by a periscope which adjusts the beam diameter in a way that it has about the same size as the light in the FSF cavity. The position and the direction of the seed laser can be adjusted with two mirrors to point the seed light in the exact same direction as the FSF light.
The main part of the seed light (67%, the AOM efficiency) is frequency-down-shifted in the AOM and directed to the FSF output. Only the remaining 33% are not frequency-shifted and seed the FSF laser. This light is amplified by passing through the gain crystal and is frequency-up-shifted in the AOM. The light that is not frequency-shifted in the AOM will exit the FSF laser towards the Michelson interferometer. In order to reduce the optical bandwidth, a narrow bandwidth optical filter was inserted into the cavity for some measurements. This setup results in a system mathematically described in Chapter 2.

The main items in the FSF laser were

- **Verdi-V5** from *Coherent*: pump laser for the TiSa
- TiSa crystal: 2.9mm long
- **MT300-B20A0.5-800** from *AA Opto-Electronic*: the AOM with a carrier frequency of 300MHz ±10MHz. Its maximum RF power is 1.5W, and its diffraction efficiency was measured as 67%.
- **LL01-780-12.5** from *Semrock, Inc.*: the narrow bandwidth optical filter with a transmission at 780nm. The wavelength of the transmission maximum can be

slightly changed by tilting the filter.

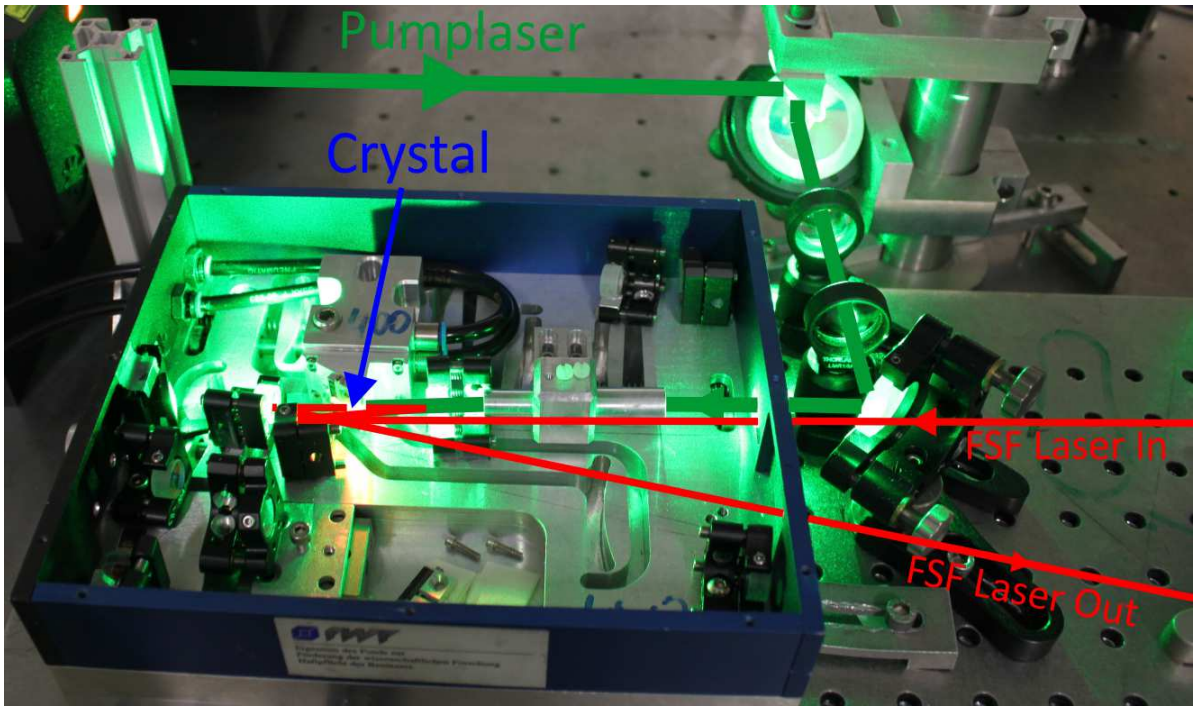


**Figure 3.6.:** FSF laser near the TiSa crystal.

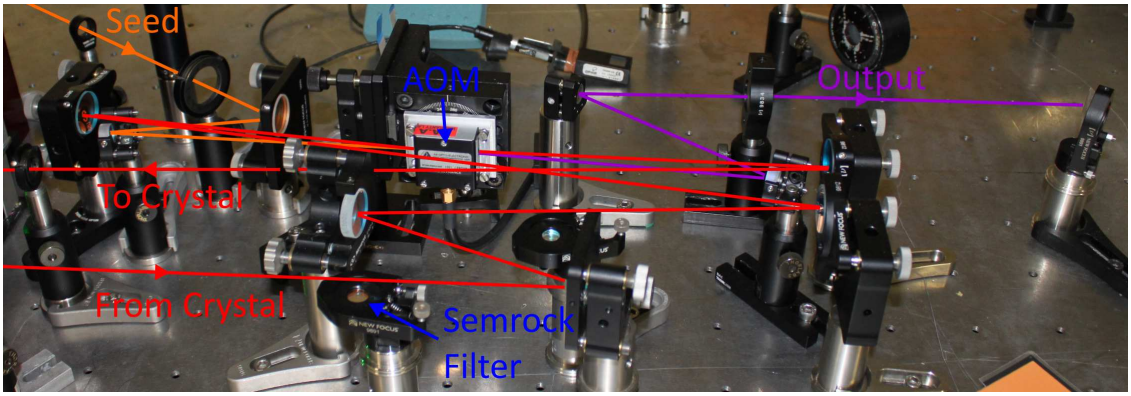


**Figure 3.7.:** FSF laser near the AOM, where one can see the in-coupling of the seed light and the out-coupling of the FSF output.

As already mention, I had already built an FSF laser in my previous thesis and the optical setup only had to be altered. For a more detailed description on the FSF laser part, I would like to refer the reader to this thesis [16].

## 3.3 Michelson interferometer

The Michelson interferometer with a high-reflector target can be seen in Figure 3.1. A beam splitter (BS) splits the incoming light into two beams which are both reflected back. The BS combines these two reflected beams again. This combined beam is detected using a photodiode (PD), and the RF spectrum is measured. One of the mirrors is on a translation stage so that the distance in one arm, the measurement arm, can be varied.
Unfortunately, this simple setup cannot be used when working with a diffusely scattering target. The heterodyne beat measurement is very sensitive to angular mismatch [26]. Hence, the beams of both arms have to be combined collinearly to observe the beat signal in the RF spectrum. The light at diffuse target scatters the light in a solid angle of $2\pi$. Only very little of that scattered light will be collinear to the light from the other arm, the reference arm. Therefore, a heterodyne beat signal cannot be observed. A setup that allows a diffusely scattering target in the measurement arm can be seen in Figure 3.8.

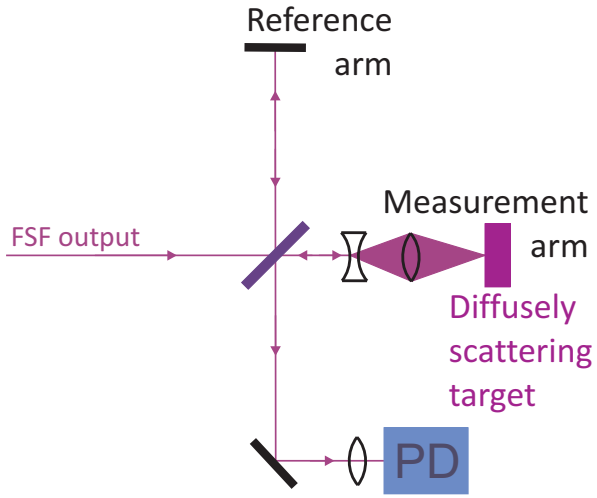


**Figure 3.8.:** Michelson interferometer setup suitable for a diffusely scattering target

In this setup, the reference stays a regular high-reflector mirror. In the measurement arm, there is a concave lens to broaden the beam. Behind the concave lens, there is a convex lens at the point at a position where the beam nearly fills up the whole convex lens. And roughly in the focal point of this beam behind the convex lens, the diffusely scattering target has to be. The light at the target is scattered into a solid angle of $2\pi$. But all the light passing the convex lens again is focused towards the concave lens which converts this light to a beam that is collinear to the other beam at the PD. That means the efficiency of this setup only depends on how much solid angle the convex lens covers seen from the diffusely scattering target.
The following figure shows the actual setup in the lab of the Michelson interferometer for the high-reflector target and the diffusely scattering target.

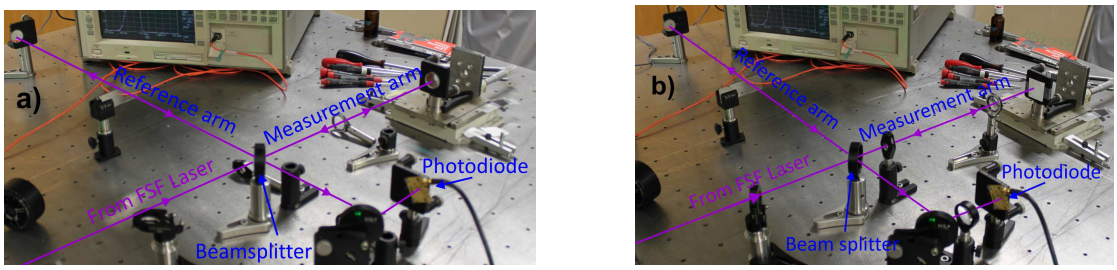


**Figure 3.9.:** Setup of the Michelson interferometer for a high-reflector target a) and for a diffusely scattering target b).

# 4 Experimental results

The chapter focuses on the optical properties of the FSF laser system, and mainly on the distance measurement done with this laser system. The pieces of equipment used in these experiments were

- **Fieldmaster LM-10 HTD** from *Coherent*: the optical power meter for higher optical intensities,
- **Orion PD300-UB** from *Ophir Photonics Group*: the optical power meter for lower optical intensities,
- **AQ-6315A** from *Yokogawa*: the optical spectrum analyzer,
- **FSP Spectrum Analyzer 9kHz .. 3GHz** from *Rohde & Schwarz*: the RF spectrum analyzer,
- **E4424B 250kHz-9GHz ESG - AP Series Signal Generator** from *Agilent Technologies*: frequency generator used for the RF signal driving the AOM,
- **81150A 120MHz Pulse Function Arbitrary Generator** from *Agilent Technologies*: arbitrary function generator used to generate the EOM modulation frequency,
- **SMU 200A Vector Signal Generator** from *Rohde & Schwarz*: the vector signal generator (VSG) used to generate the EOM modulation signals needed in chapter 4.4 (this device was on loan from the "Institute of Telecommunications" of the UT Vienna for these measurements).

## 4.1 Optical properties of the FSF laser system

In Figure 4.1, one can see the optical power output characteristics of the laser system. It has a threshold pump power of 3.25W and a maximum output power of about 240mW.

The optical spectrum for the unseeded case shown in Figure 4.2 is similar to the one reported in [16]. With no filter, the full width half maximum (FWHM) optical bandwidth was measured to be approximately 5nm. The Semrock filter reduced the optical bandwidth to about 0.2nm.
The AOM in the cavity was aligned so that a frequency-up-shift was obtained. That means that the wavelength was reduced after each round trip. Hence, the seed must have a longer wavelength than the unseeded FSF laser for optimal seeding. If that is

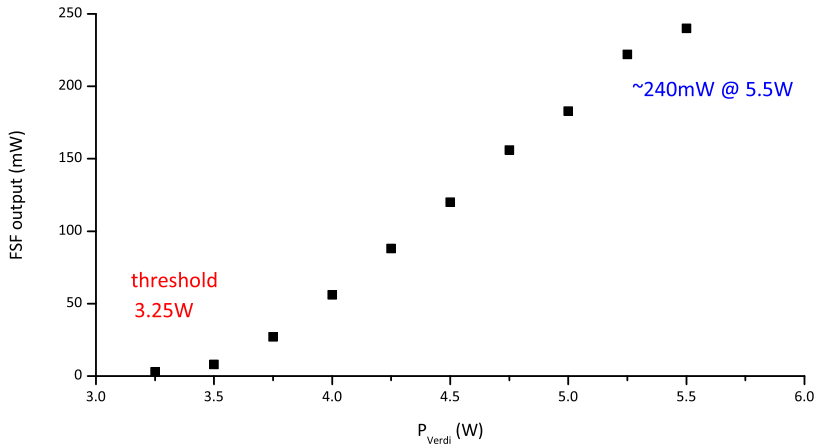


**Figure 4.1.:** Optical output power in dependence of the pump power

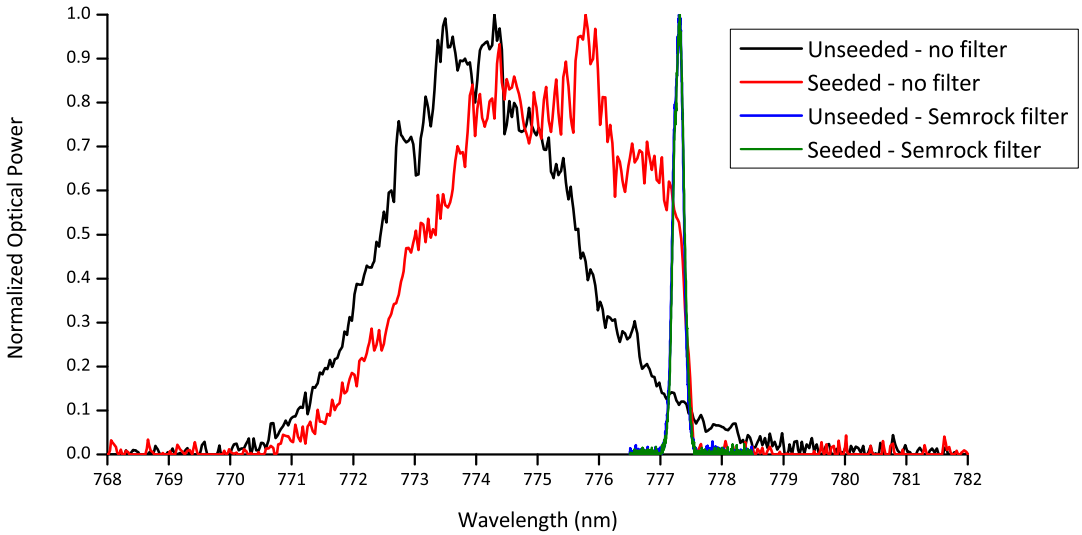


**Figure 4.2.:** Optical spectra of all used configurations of the laser system

guaranteed, a spectrum similar to the ones seen in Figure 4.2 will be obtained. In the seeded case, the optical intensity starts abruptly at the spectral position, where the FSF laser is seeded, unlike to the unseeded case, where the intensity increases gradually. The FWHM bandwidths are approximately the same with or without seeded. But in the seeded case, a frequency comb forms. Unfortunately, the resolution of the optical spectrum analyzer is not sufficient to actually resolve the individual comb lines.

### 4.1.1 RF spectrum of the seed light

It is mandatory to know the spectrum of the seed light because one has to make sure that the seed light has the desired optical properties. Due to the setup of the seed laser system, it is known that the PPLN produces light of 777.5nm wavelength. But one would need a high resolution optical spectrum analyzer to resolve the optical spectrum with RF resolution at this wavelength. Such an optical spectrum analyzer was not available.

Fortunately, the exact, absolute position of the seed laser frequency is not important for this measurement. It is only necessary to have a narrow central peak (at 1555nm) which is phase modulated and exhibits side bands. One can use this knowledge to do a simple measurement with a photodiode directly in the output beam of the PPLN to verify this spectrum. For the measurement, the EOM was modulated with a frequency of 20MHz and a peak-to-peak amplitude of 2V. The resulting RF spectrum on the photodiode can be seen in the following figure.

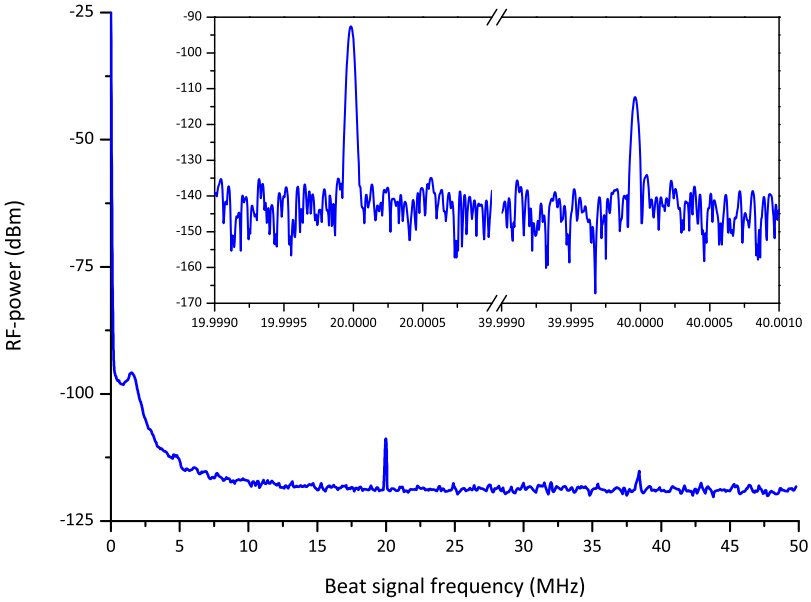


**Figure 4.3.:** Measurement of the RF spectrum of the seed light with a modulation frequency of 20MHz and an amplitude of $2V_{pp}$

Unfortunately, the RF spectrum analyzer did not support DC voltages. Hence, a DC block had to be used. It had a cut-off frequency of ∼10MHz. That explains the rising signal towards 0Hz.

The measured signal is an autocorrelation of the electric field of the seed laser output. In the optical spectrum, we expect a line from the SFL and other lines on each side of the SFL line separated by the modulation frequency and its harmonics. In the RF spectrum, one should see the beat signals created by these lines. And this is what we observe in Figure 4.3. Due to the DC block, the peak at 0Hz cannot be uniquely associated with the autocorrelations of the spectral peaks with themselves. But we can see a spike at 20MHz, the modulation frequency. This is where spectrally neighboring peaks create a beat signal in the PD. We even observe the second harmonic, where a peak forms a beat with its second neighbors. The second harmonic has an amplitude reduced by 20dB compared to the peak at the modulation frequency. That means that the higher harmonics are in the beat spectrum, and one has to make sure that they do not create signals which interfere with the distance measurement.

## 4.2 High-reflecting mirror as a target

### 4.2.1 Distance measurement

The theory in Chapter 2 predicts that the measured peaks of the autocorrelation would be at the multiples of the free-spectral range $f_{FSR}$ of the FSF laser. And there should be two distance-dependent RF beat signals between two autocorrelation peaks. This is exactly what is observed in the following figure.

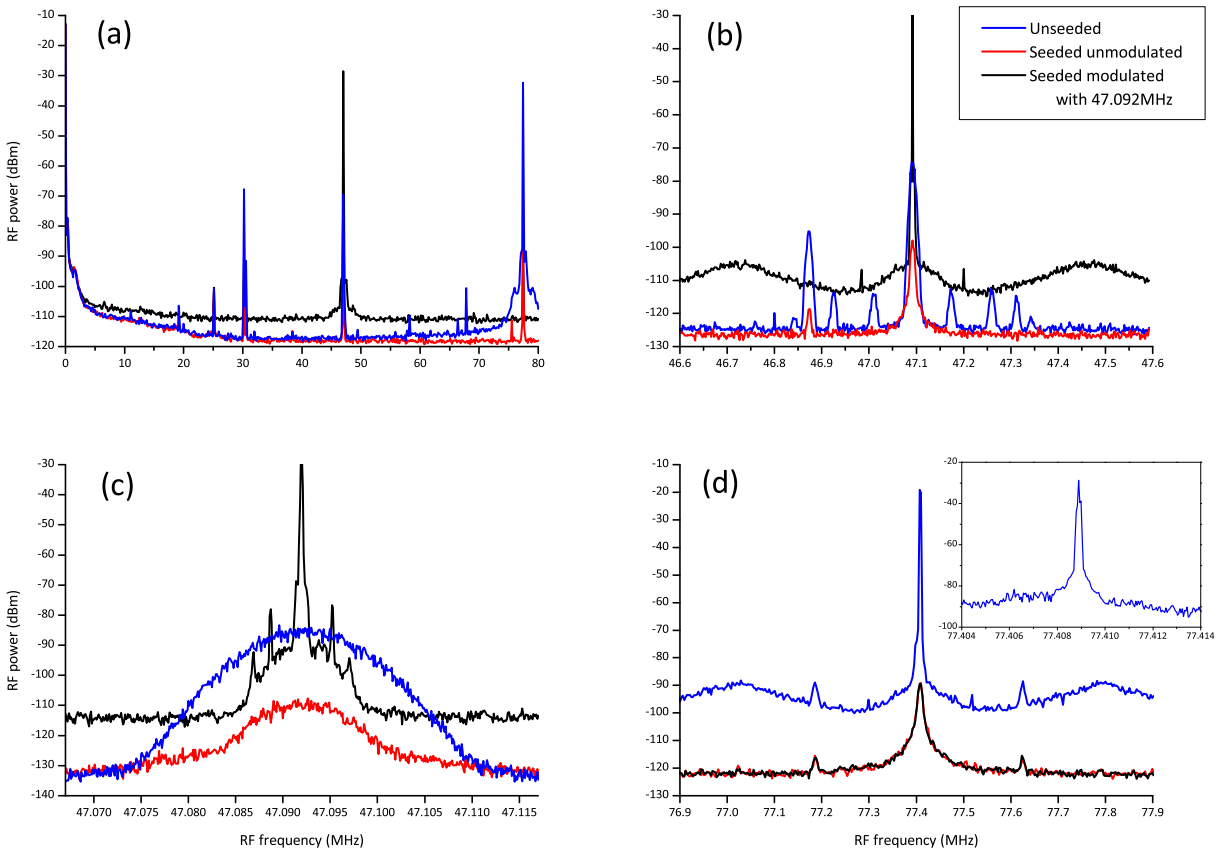


**Figure 4.4.:** The panels (a)-(d) show different frequency ranges of the RF spectrum for various seeding conditions. (a) represents the RF spectra from 0-80MHz, where one can see the two distance-dependent peaks and the peak of the FSR. (b) and (c) exhibit the distance-dependent peak with a span of 1MHz and 50kHz. (d) shows the peaks of the FSR with a span of 1MHz and high-resolution zoom to picture the cavity FSR more accurately.

Panel (a) shows the RF spectrum from 0 to 80MHz. The rising signal towards 0Hz is again caused by the DC blocker. The first distance-dependent peak can be seen between 30 and 31MHz. This peak can be seen in the spectra of all seeding types (unseeded, seeded but unmodulated, seeded with 47.092MHz). The next distance-dependent peak is at 47.092MHz and can be seen in detail in panels (b) and (c). The autocorrelation peak is at 77.409MHz, panel (d).

If one takes a closer look at the signals for the seeded unmodulated case, one can see that

these signals never show the best SNR of the three seeding types. Hence, the properties of the seeded unmodulated signals will not be investigated any further.
In panels (b) and (c), the seeded modulated signals show a big increase of more than 50dB in the beat signal amplitude compared to the unseeded case. That is exactly what the aim of the seeding was, increasing the SNR.
The peak corresponding to the cavity FSR in panel (d) has a smaller SNR for the seeded case than for the unseeded case. That is not surprising because the seeded signal was designed to have the best SNR for the distance-dependent peak. In the inset in (d), one can see a detailed zoom of the FSR peak for the unseeded case. With that, $f_{FSR}$ can be determined to be 77.409MHz, which corresponds to an optical path length of 3.873m.
**Comment:** The small peaks near the main peaks are caused by weak reflections. For example, even if one uses a BS with anti-reflection (AR) coating, a small fraction of the light will still be reflected at the AR-coated surface. This will correspond to a different path length in the Michelson interferometer which can be seen in the RF spectrum.

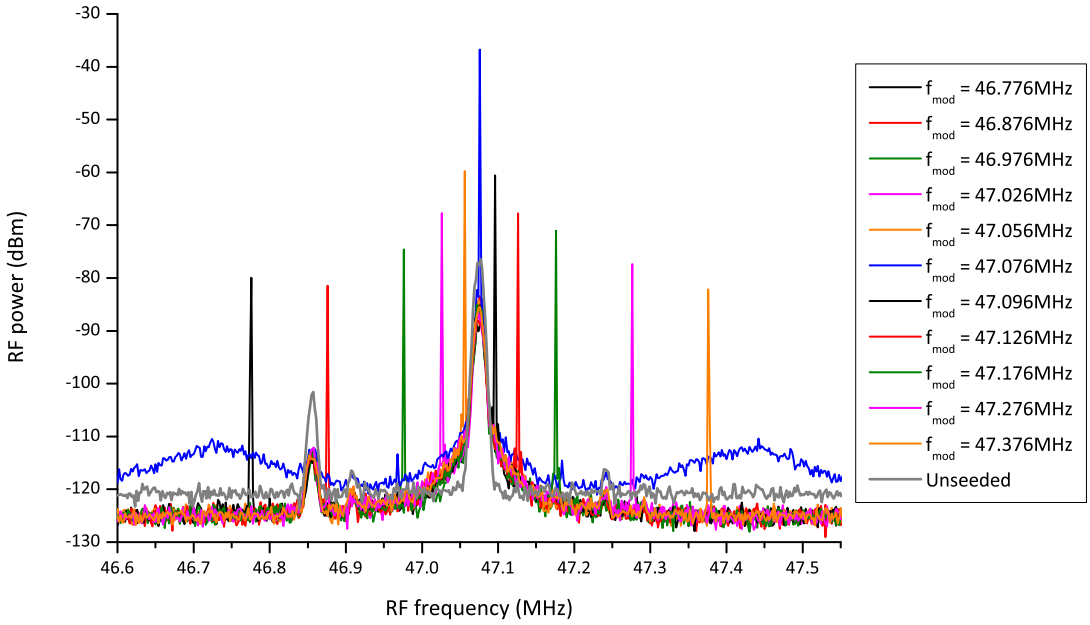


**Figure 4.5.:** Scanning of the modulation frequency for distance measurements. The frequency with the highest beat signal corresponds to the distance to measure.

The distance of the measurement arm was 37cm and that of the reference arm 67cm, both measured with a ruler. Hence, the distance difference was approximately 30cm. The exact value can be calculated with the frequencies observed in Figure 4.4 by rearranging Eq. (2.40) and $\lambda_2 = 0$. Hence,

$$L = \frac{f_{mod}}{f_{FSR}}\, L' = \frac{47.092\text{MHz}}{77.409\text{MHz}}\, \frac{299792458\text{m/s}}{2 \cdot 300\text{MHz}} = 0.303966m = 30.3966cm \tag{4.1}$$

where the modulation frequency $f_{mod}$ corresponds to the EOM frequency $f_{EOM}$.

To perform distance measurements, one has to scan the modulation frequency. The frequency with the highest distance-dependent peak amplitude corresponds to the distance

to measure, as discussed in Chapter 2. Figure 4.5 shows the RF spectra for various modulation frequencies $f_{mod}$ around the distance-dependent beat frequency. One can see that the modulation frequency always appears in the RF spectrum. If the modulation frequency and the spectrum for the unseeded case do not match, the peak of the modulation frequency will still be 45dB above the noise floor. But if they match, the peak will be 90dB above the noise floor and the SNR compared to the unseeded case will increase by a factor of 45dB. Even if the modulation frequency is off by just 20kHz compared to the value of the highest peak, the SNR will drop by 25dB. This sensitivity and the high SNRs make high-precision distance measurements possible.

To demonstrate distance measurements, the distance of the measurement arm was changed, as shown in Figure 4.6. Distance 1 corresponds to the previous 30.3966cm according to Eq. (4.1). For Distance 2, the distance was increased by 1cm with the micrometer of the translation stage. $f_{mod}$ of 48.640MHz complies with a distance of 31.3958cm. For Distance 3, the distance of Distance 1 was decreased by 100$\mu$m. In that case, $f_{mod}$ of 47.076MHz complies with a distance of 30.3863cm.

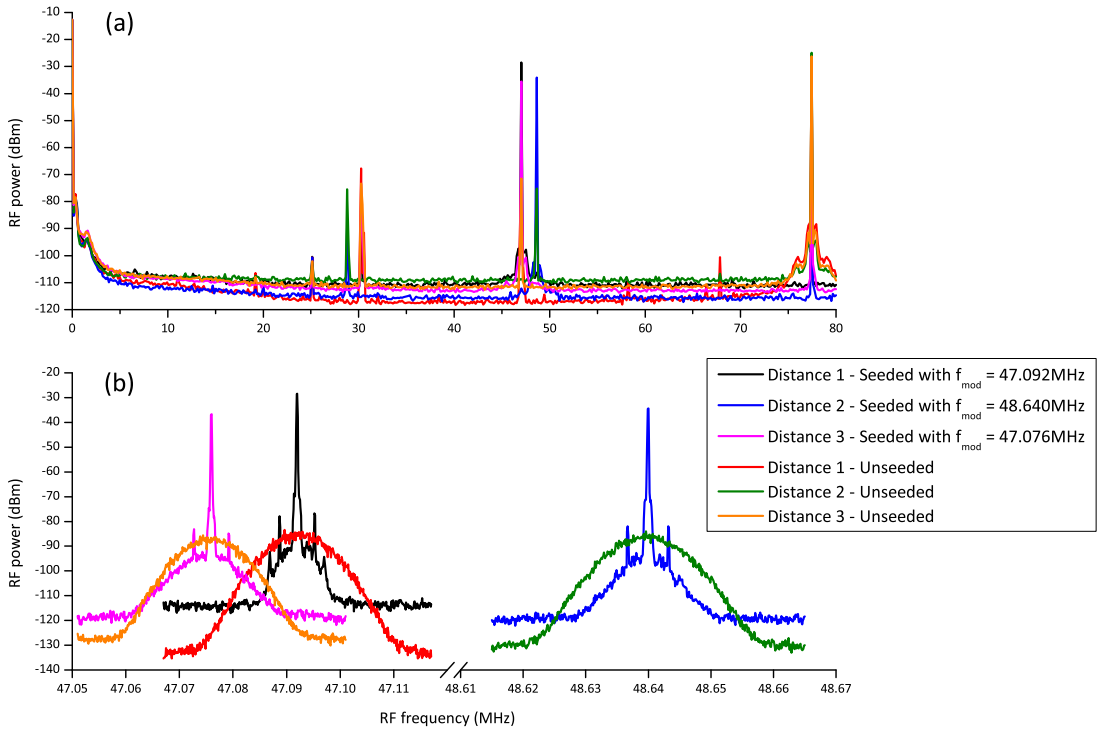


**Figure 4.6.:** RF spectra for three distances for the seeded and the unseeded case. (a) represents the RF spectra from 0-80MHz, and (b) represents the zooms of the distance-dependent peaks each with a span of 50kHz. Distance 2 corresponds to a distance increase of ≈1cm compared to Distance 1. And for Distance 3, Distance 1 was decreased by ≈100$\mu$m.

**Comment:** In this chapter, all frequencies are stated with an accuracy of 1kHz because due to the spectral width of the unseeded case (Figure 4.4 (c)), it was possible to determine the center frequency with an accuracy of 1kHz. That corresponds to a distance resolution

of 6.5$\mu$m. Hence, all these distance measurements were done with this resolution.

### 4.2.2 Dependence on modulation amplitude

In the beat intensities, Eq. (2.14 - 2.16), one can see a dependence of the created beat signal from the modulation amplitudes through the Bessel functions and their arguments, Eq. (2.17 - 2.19). This dependence is experimentally proven in this chapter.

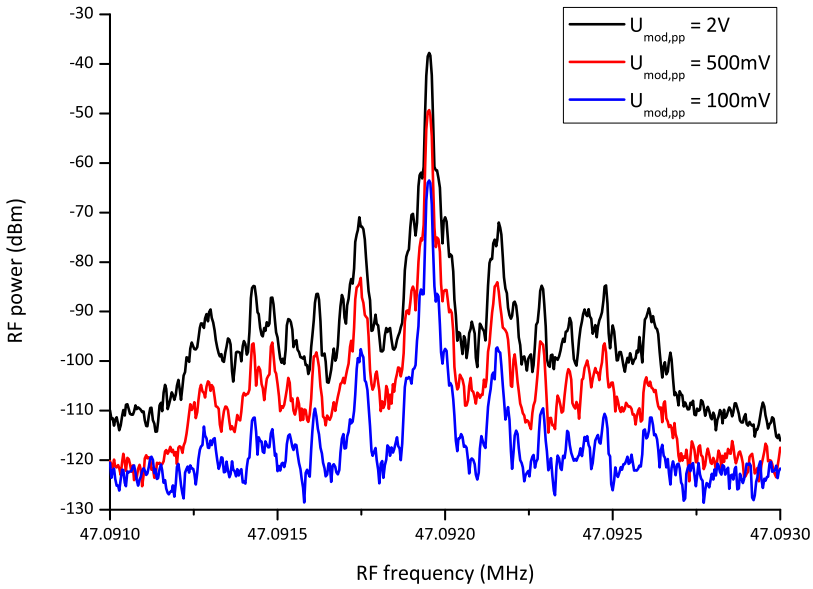


**Figure 4.7.:** distance-dependent RF beat signal for various modulation voltages (resolution BW 10Hz).

In Section 2.3.3, the restriction on the number of sidebands $n = 1$ was made for these measurements, meaning the only remaining Bessel functions in Eq. (2.14 - 2.16) are $J_1$ and $J_2$. In Figure 4.7, one can see an increase in the beat signal amplitude with rising modulation amplitudes. That means, the first maximum of the Bessel functions was not yet reached, otherwise the amplitude would decrease for higher modulation amplitudes. That implies that one can use high modulation amplitudes to increase the SNR of the signal. There is one disadvantage of high modulation amplitudes, though. Higher modulation amplitudes will cause higher Bessel functions, too, and the restriction $n = 1$ may no longer be valid. That would mean that for higher modulation amplitudes, there will be peaks at $2f_{mod}$ and even higher harmonics, similar to what was already mentioned in Section 4.1.1. Hence, if $2f_{mod}$ matches the distance-dependent peak, there will be a peak with good SNR at $2f_{mod}$.
Fortunately, this effect is suppressed due to using the SHG-PPLN. The harmonic of a sideband after the phase modulation corresponds to the order of the Bessel function. The amplitudes of the sidebands next to the central peak are proportional to $J_1$, their neighbors to $J_2$ and so on. Since SHG is sensitive to light intensities, the weaker sideband amplitudes will decrease in relation to the amplitude of the central peak.

### 4.2.3 Influence of the optical bandwidth

For many applications, the distance measurement should be done in the fastest way possible. When the modulation frequency is mixed into the seed light, one has to wait until the whole spectrum of the FSF laser is filled with light of that specific modulation frequency before the beat signal measurement can start. Hence, measurements with smaller optical bandwidths can be done with less waiting time, thus faster, compared to larger optical bandwidths. In this Section, a Semrock laser line filter was inserted into the cavity to intentionally reduce the optical bandwidth of the FSF laser. The different optical spectra are the ones from Figure 4.2. The measurements with and without the filter are compared in the following Figure 4.8.

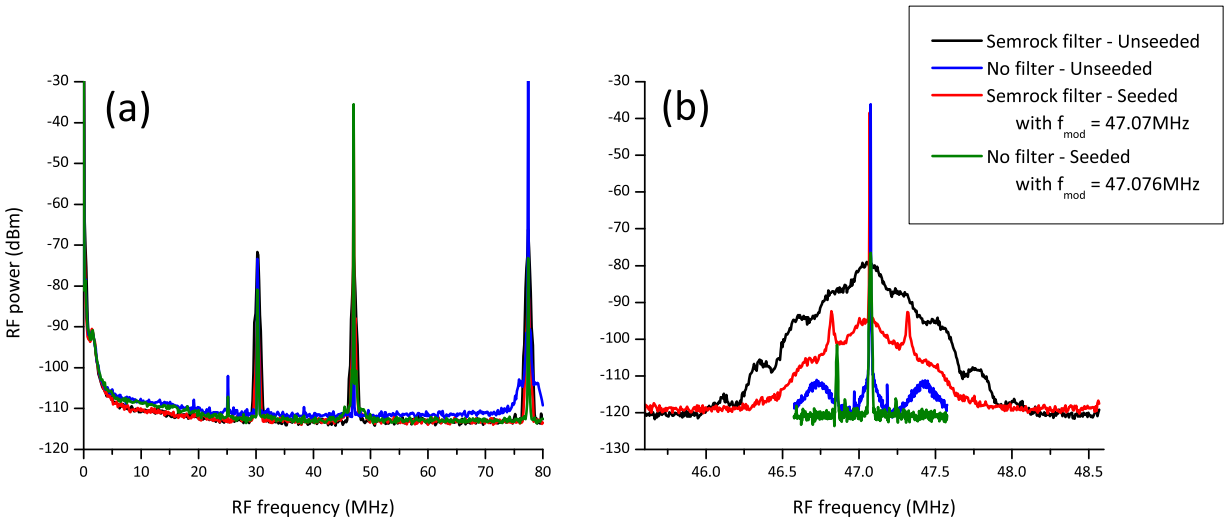


**Figure 4.8.:** RF spectra for two different optical spectra of a seeded and an unseeded laser. (a) shows the RF spectra with the pairs of distance-dependent peaks and the FSR peaks. (b) shows the zoom of the distance-dependent peaks.

Naturally, there is change on the position of the peaks in the RF spectrum for different optical spectra. But narrower optical bandwidths correspond to broader RF beat signals, as theoretically shown by Yatsenko *et al.* [17], compare Eq. (37). The width of the beat signal is inversely proportional to the number of comb modes, thus inversely proportional to the optical bandwidth of the FSF laser. The unseeded RF beat signal without the filter had a total width above the noise floor of 35kHz (FWHM of ≈7kHz). The one with the filter had a total width of ≈2MHz (FWHM of ≈25kHz). One can see that seeding with and without filter increases the SNR drastically. But for the case with the filter, some energy remains in the broad pedestal and therefore the peak is not as high as the one without the filter and the narrow pedestal.

In Figure 4.9, the modulation frequency was detuned for the case with the Semrock filter. The results are similar to the ones shown in Figure 4.5. But the beat signal is much broader now. This makes it difficult to determine the modulation frequency with the highest SNR accurately. And it decreases the achievable distance resolution. This is

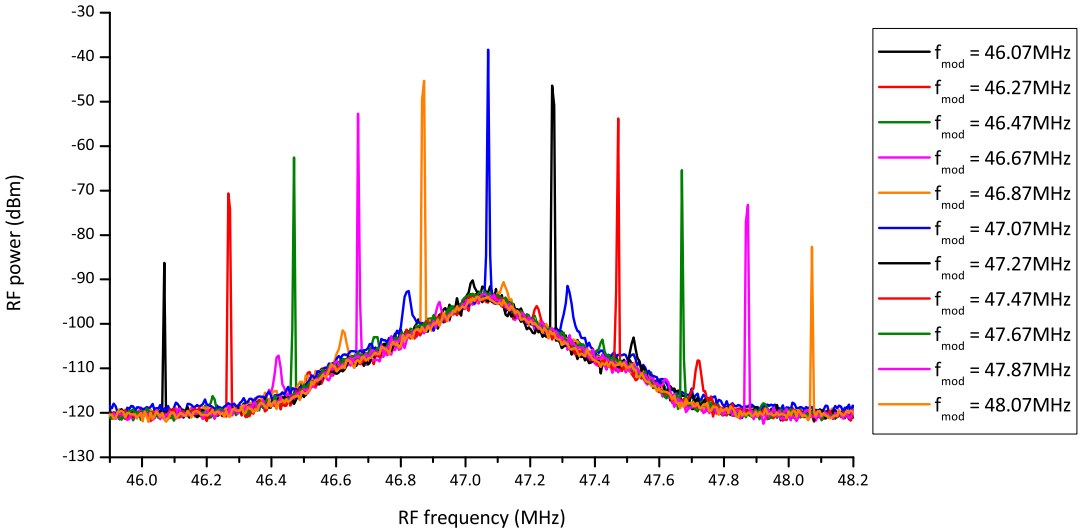


**Figure 4.9.:** Scan of the modulation frequency. The achievable distance resolution is reduced due to the reduced optical bandwidth.

not surprising because if one wants to measure distance more accurately using the same measurement principle, the measurement duration will increase. For the real-time distance measurement system, one has to find a trade-off between desired distance resolution and desired frame rate (measurement duration).

## 4.3 Diffuse target

As mentioned in Section 3.3, a different setup including a lens system in the Michelson interferometer has to be used to obtain a beat signal with a diffuse target.

### 4.3.1 Comparison of beat SNR with and without seed

A diffuse target reduces the SNR drastically, because not all of the light is reflected and not all of the reflected light ends up collinearly to the beam from the reference arm in the PD. Figure 4.10 shows the RF spectra for the unseeded, the seeded unmodulated, and the seeded modulated case. The seeded unmodulated case exhibits again the worst SNR because no distance-dependent signal can be detected. In the unseeded case, the SNR is just 5dB and has a total width of ≈25kHz (FWHM of 300Hz). This SNR is too low for reliable distance measurement. Hence, the signals of the seeded unmodulated and the unseeded cases will be neglected for the rest of this section.
The SNR of the seeded modulated case is 55dB and has a width smaller than 1kHz (resolution BW 100Hz).

Reliable distance measurements with this SNR are possible and will be shown later in this chapter.

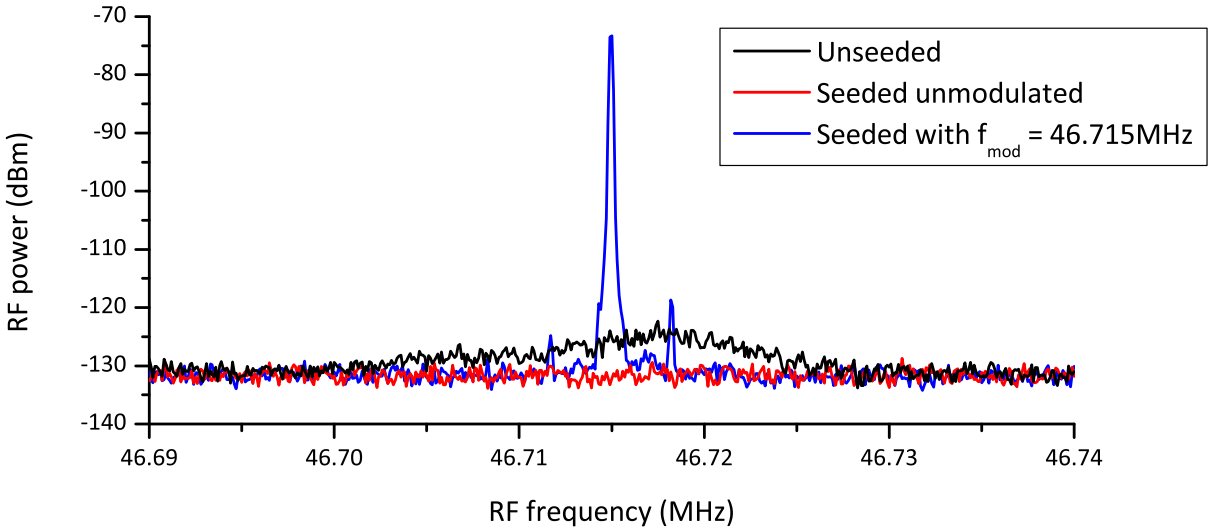


**Figure 4.10.:** Beat signals for unseeded and seeded cases for a white paper target. Only when the FSF laser is seeded and modulated with the correct modulation frequency, the beat signal can be used for distance measurement, because it has a SNR of 55dB.

### 4.3.2 Finding the optimal seed modulation frequency

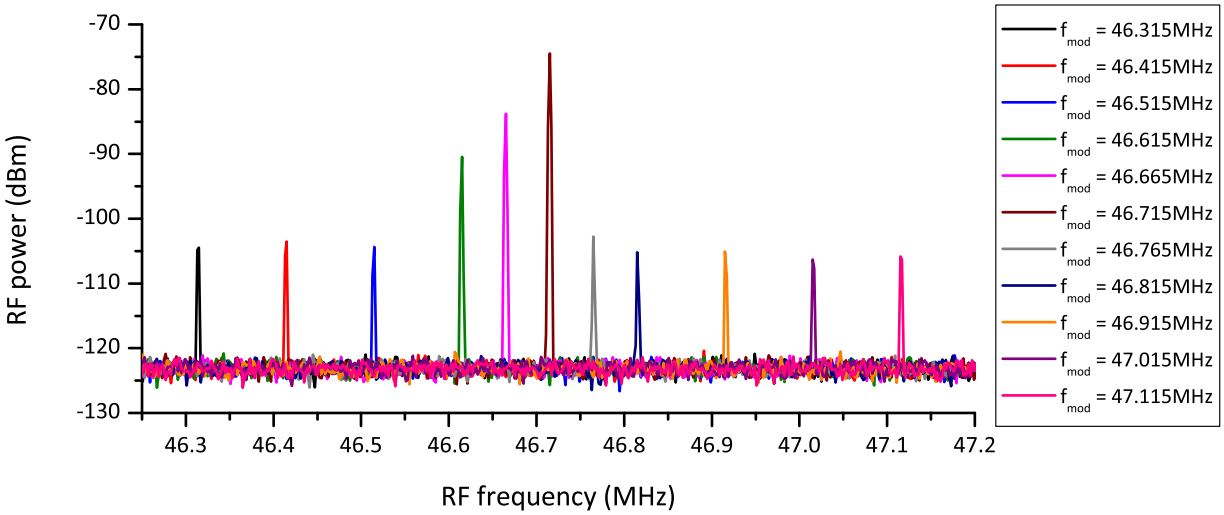


**Figure 4.11.:** RF spectra for white paper target for various modulation frequencies.

Optical radiation can penetrate the white paper target. Hence, many layers of the paper will reflect light. Figure 4.11 shows the RF spectra for various modulation frequencies. Since the white paper was put in front of a high-reflector, the light that passed through the paper was reflected back and again scattered by the paper. The highest beat frequency was found at 46.715MHz, and in a range of about 200kHz the beat signal is enhanced. With these results, distance measurement will be possible. One can even see the shape of the reflecting layers of the paper in the beat spectra, too.

### 4.3.3 Different distances

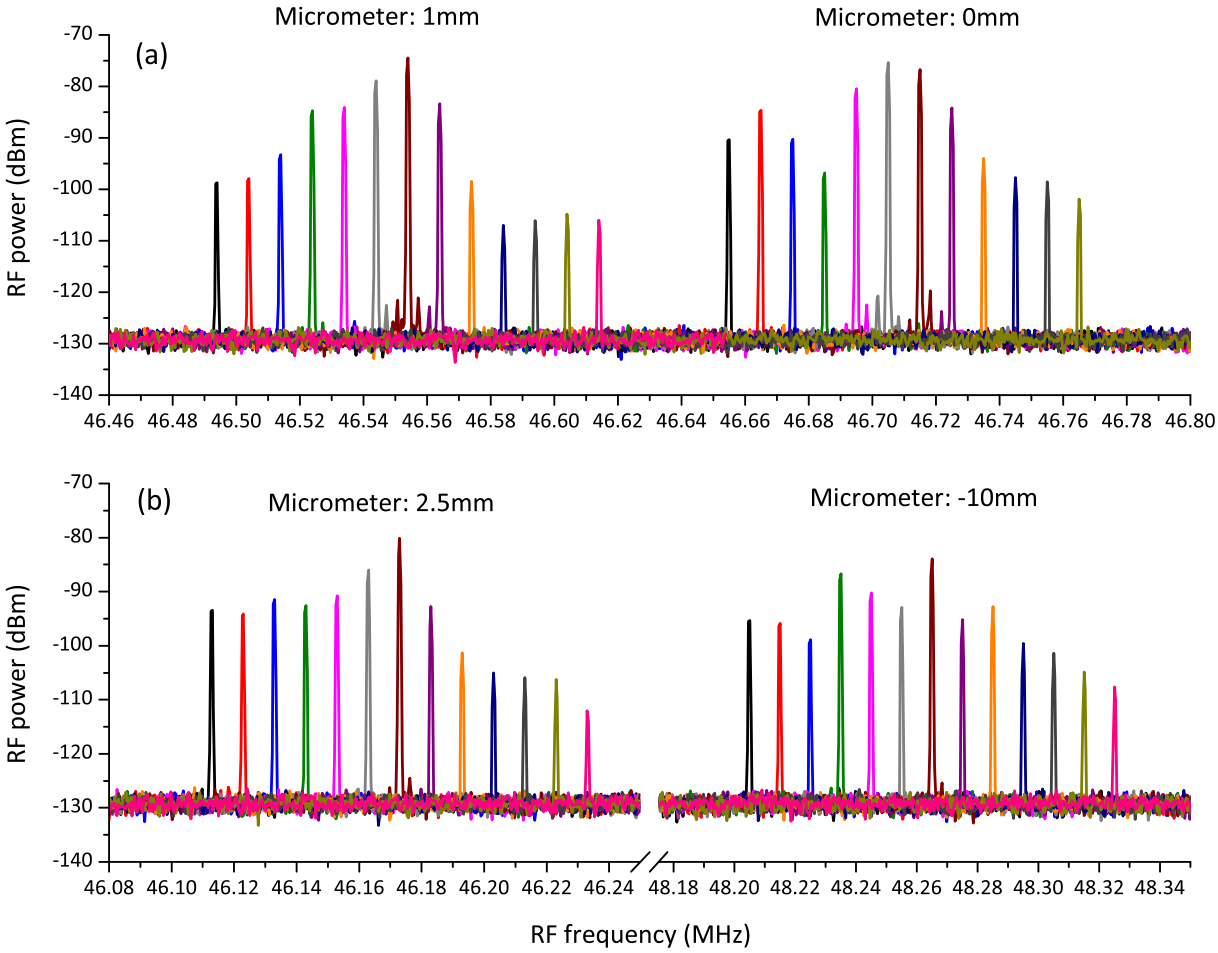


**Figure 4.12.:** RF beat signals for various modulation frequencies for a white paper target at four different distances.

The white paper target was placed at four distances with the micrometer from the translation stage. The RF spectra for various modulation frequencies at the four distances can be seen in Figure 4.12. The shape of the reflecting layers of the paper in the beat spectra changes slightly for the different distances, because if the focused light hits another spot on the white paper, the reflection and transmission will be different.
Since these distinct spectra correspond to different path lengths, they allow us to recover the distance information and thereby distinguish between different distances.

### 4.3.4 Different targets

| **Target** | **SNR / dB** | $f_{mod}$ **at the peak / MHz** |
|---|---|---|
| White paper | 60 | 46.701 |
| Yellow paper | 57 | 46.706 |
| Black paper | 40 | 46.706 |
| Mirror (with imaging setup) | 76 | 46.659 |
| Black cardboard | 38 | 46.798 |
| Black plastic | 30 | 48.310 |

**Table 4.1.:** SNR and the corresponding modulation frequencies of the beat signal for various targets.

To demonstrate distance measurements with more than one type of diffuse targets, various targets were put into the measurement arm. Table 4.1 shows the SNR of the beat signal these targets caused at a given modulation frequency. The worst SNR was found for the black plastic. But a SNR of 30dB is still enough for reliable distance measurements.

## 4.4 Measurement with pre-set distance resolution

In [23], we performed measurements where we could pre-set the distance resolution of our measurement process. In the measurements discussed in the preceding Sections, a narrow seed was phase-modulated with a modulation frequency that was tuned in regular steps. But if one uses too big steps (for high distance resolution), then it can happen that there will be no overlap between the seed laser peak and the distance-dependent peak. Hence, no frequency will be enhanced and a wrong frequency might be detected as the distance-dependent frequency.
One solution to solve this is to use a seed laser with a linewidth broader than the biggest desired frequency step. But that has the disadvantage, that a lot of the light does not contribute to the beat frequency. Only the narrow part, where the seed laser modulation frequency and the distance-dependent peak frequency overlap, contributes. This reduces the SNR of the detected signal.
In order to pre-set the distance resolution, as proposed in [23], we used a narrow seed and did the phase modulation not with a single frequency but with a frequency range of a well-defined center frequency $f_{center}$ and well-defined width. This width is created by adding white noise around the center frequency and is therefore called noise bandwidth ($NBW$). It corresponds to the desired distance resolution through the formula

$$\Delta L\,(NBW) = \frac{NBW}{f_{FSR}}\; L' = \frac{NBW}{f_{FSR}}\;\frac{c_0}{2\,f_{AOM}} \qquad . \tag{4.2}$$

To cover the whole RF spectrum, the center frequency has to be detuned in steps of $NBW$. This makes sure that the whole RF spectrum is covered during one measurement

cycle of scanning $f_{center}$ and that as much light as possible contributes to the beat signal. Hence, the best SNR for a given distance resolution is reached.
With this technique, one can decrease the time of one measurement cycle, too. At first, one sets the $NBW$ to obtain the desired distance resolution and then measures the RF spectrum. In order to resolve the ambiguities, one will normally have to detune the AOM frequency and measure all modulation frequencies again. With this technique, one can resolve the ambiguity with much longer distance resolution (bigger frequency steps). Thus, one measurement cycle will contain fewer measurements to obtain the same information[1].

If one only has one pixel, or one knows that the distances for all pixels will be close to each other, then one can take this even one step further. One could use successive approximation to get to the right distance measurement result. For successive approximation, one chooses the $NBW$ to be half of the full frequency range to determine, in which half the target is. Then one splits the half frequency range, in which the target is, in two parts and repeats the measurements with a $NBW$ half as big as before. This splitting and measuring is repeated until the desired distance resolution is reached. This reduces the number of frequency steps $n$ per cycle to $lb\ n$. Unfortunately, this cannot be generalized for multipixel systems because the targets for the individual pixels can be in completely different positions. One would need a frequency source for each pixel to make use of successive approximation with multiple pixels.

If not otherwise stated, the setup in the Michelson interferometer is the one without the additional lenses. And since some of the measurements were already reported in [23], some figures may look similar the ones in the *Optics Letters* publication.

### 4.4.1 RF spectra of the EOM modulation frequency

Normal frequency generators cannot generate the frequency spectrum described in Section 4.4. But the **SMU 200A Vector Signal Generator** (VSG) can be programmed to create such an output. The VSG was programmed to add white noise of a certain width around a center frequency and to minimize the crest factor. The generated spectra can be seen in the following Figure 4.13.

[1] This is only valid, if not all frequency steps with the short distance resolution (small frequency steps) are needed to resolve all ambiguities. But this is usually the case because the distance measurement is restricted to a certain maximum distance in which signals with good SNR are detected. And this maximum distance is normally much smaller than the distance resolvable with all frequency steps.

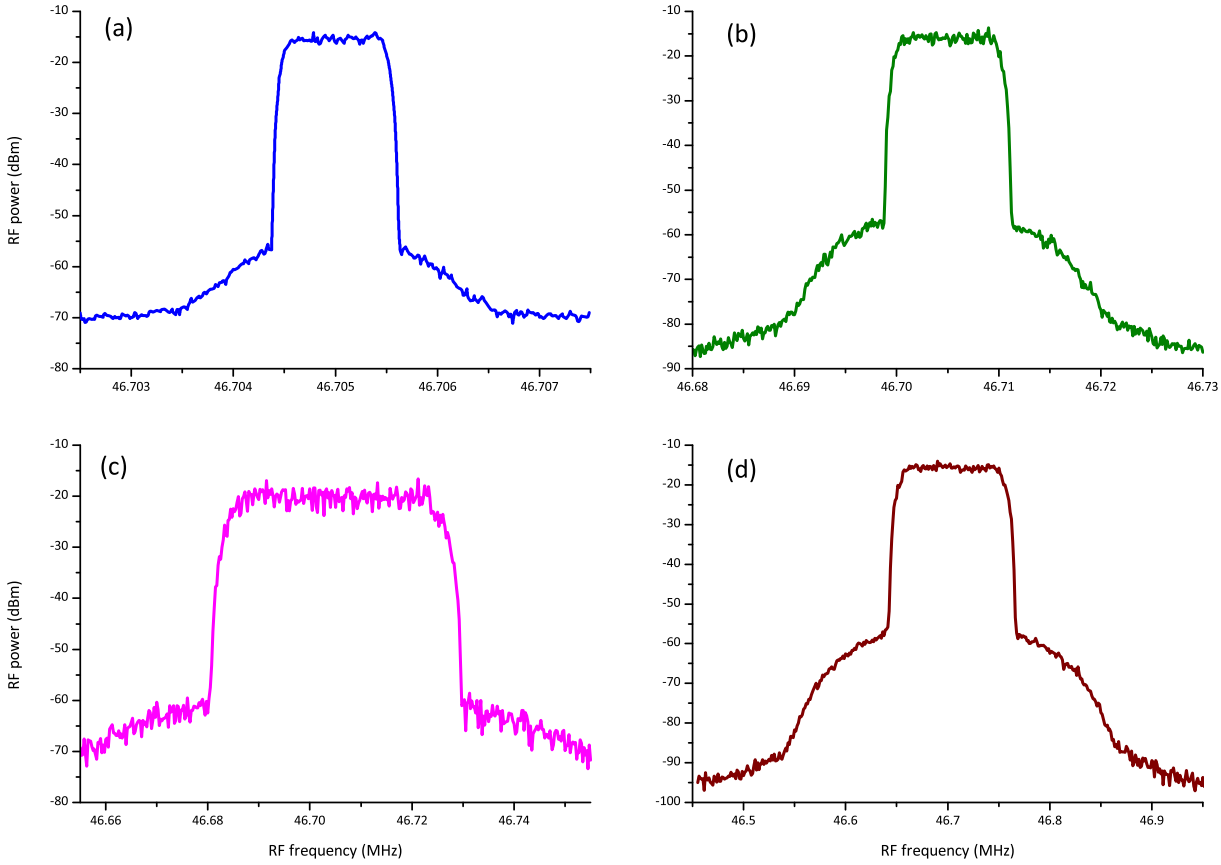


**Figure 4.13.:** EOM modulation driver signals generated with the VSG. Around a center frequency, white noise with a certain bandwidth is added. These spectra are used to modulate the light with the EOM. The center frequency in all figures is 46.705MHz. The $NBW$ is (a) 1kHz, (b) 10kHz, (c) 40kHz, and (d) 100kHz.

In Figure 4.13, one can see that the programmed width was generated very accurately. The signal drops 40dB at the edges of the modulation before its amplitudes decreases further for frequencies more distant to the center frequency.

### 4.4.2 Different noise bandwidth

In Figure 4.14 (a), one can see the beat signals where $NBW$ is smaller than the spectral width of the unseeded beat signal. In that case, the RF beat signals look similar to the unseeded case but contain the seed signals as peaks in the center.
Figure 4.14 (b) shows the case in which the $NBW$ is larger than the spectral width of the unseeded beat signal. There, the signals look similar to the seed signals but contain peaks of the width of the unseeded case in the center.

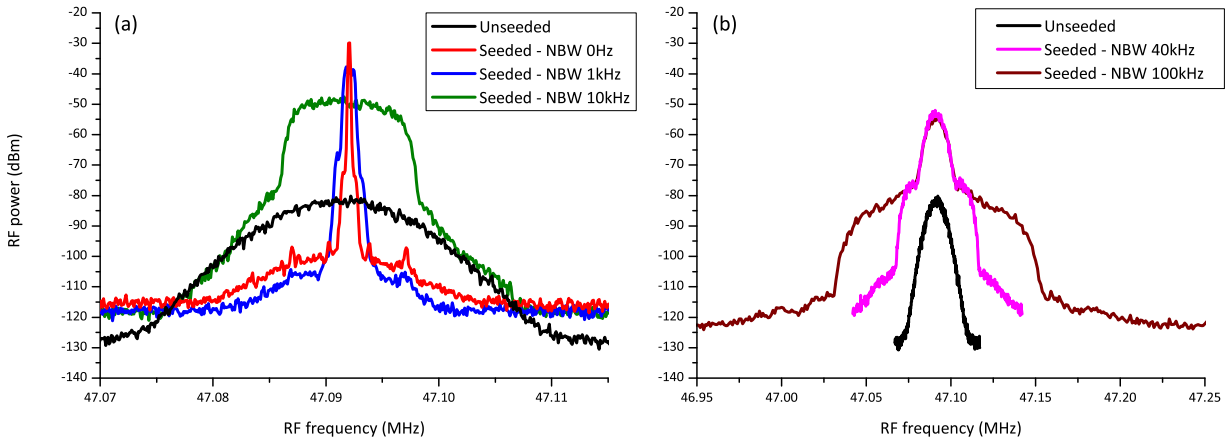


**Figure 4.14.:** In both panels, the modulation frequency was set to the maximum signal intensity at 47.092kHz. Panel (a) exhibits the RF beat signals where the $NBW$ was smaller than the spectral width of the unseeded case. (b) contains the RF beat signals where the $NBW$ was larger than the spectral width of the unseeded case.

In Figure 4.15, the beat signals for two distances separated by 1cm were measured for various $NBW$s. The RF beat signals look similar to the one in Figure 4.14 (a) only shifted when the distance was changed, as has to be expected.

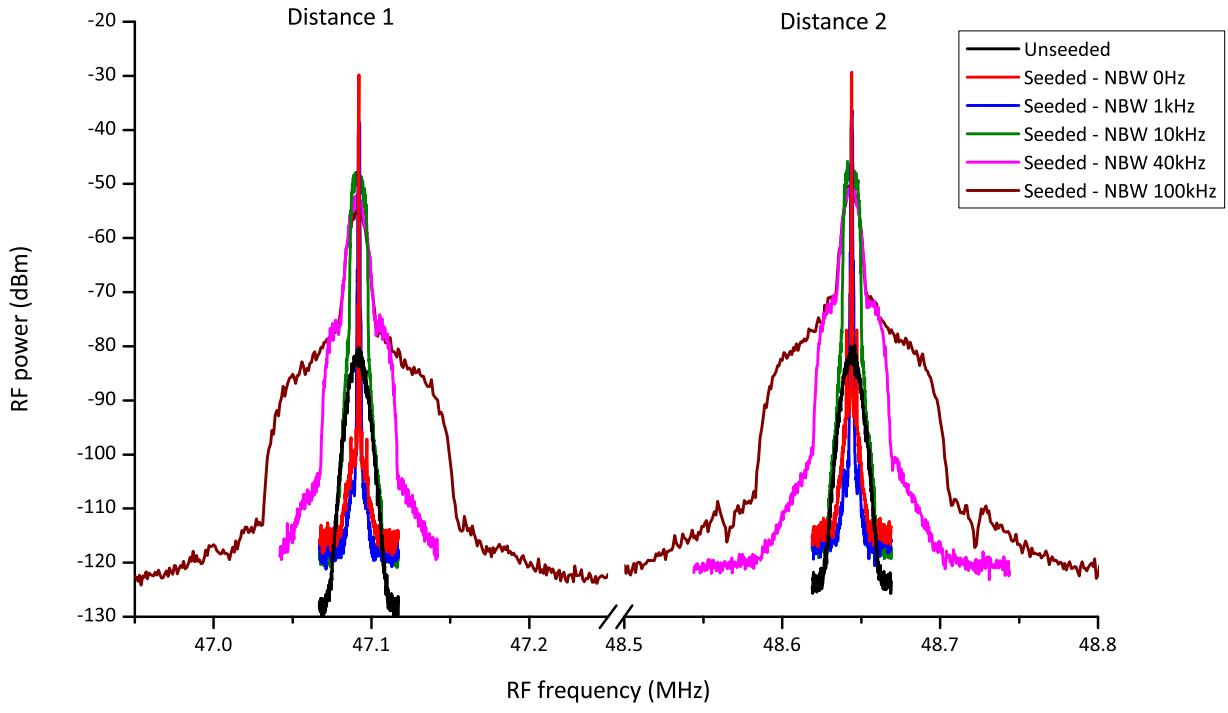


**Figure 4.15.:** RF beat signals for various $NBW$s and for two different distances. For Distance 1, the center frequency was 47.092MHz, and for Distance 2 48.640MHz.

### 4.4.3 Detuning the center frequencies

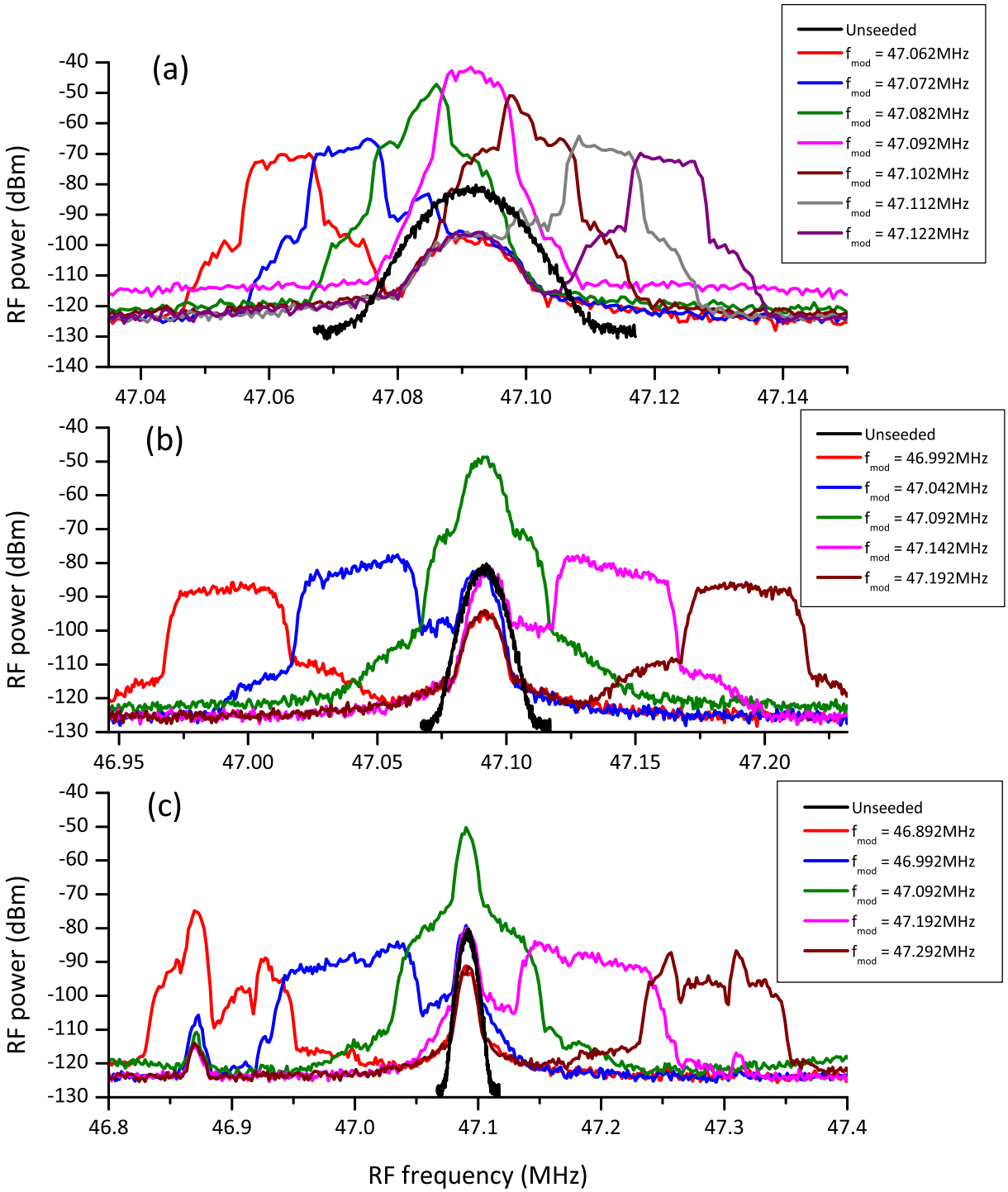


**Figure 4.16.:** In all panels, the modulation frequency was detuned from the maximum signal intensity at 47.092kHz. In panel (a) the NBW was 10kHz, in (b) 40kHz, and in (c) 100kHz.

As proposed in Section 4.4, one can detune the center frequency in steps of the $NBW$ and thereby cover the whole RF spectrum. This can be seen in Figure 4.16 for three different $NBW$s. If the center frequencies are too far detuned from the peak of the unseeded case, the beat signals will not be enhanced. Only if the seed signal and the unseeded case signal overlap, the SNR will increase and the correct distance to measure can be determined.

In [23], we reported that for single-line modulation the FWHM of the beat signals is smaller than 20Hz (limited by the measurement precision). That means that the seed laser has a line width narrower than 20Hz on our time scales[2]. - This could be determined from Figure 4.7, too, where a beat spectrum of single line modulation is depicted with a small resolution bandwidth. - Eq. (4.2) predicts a distance resolution of 129nm for the 20Hz beat linewidth. Of course, this value is only a theoretical value because one encounters similar problems as in Chapter 4.2.3. Interferometric distance measurement principles can only resolve the distance to a certain fraction of the wavelength of the light used for the measurement, as described in [17] for OFDR with FSF lasers. The optical bandwidth of the FSF laser used in the work of this thesis is too small, and thus the spontaneous-emission pedestal is too broad, to determine the height difference between two peaks, where the modulation frequencies are only separated by 20Hz. To achieve a better distance resolution, the optical bandwidth of the FSF laser should be increased. To build such a laser, one should use an AOM with higher diffraction efficiency (the efficiency of the AOM used in this thesis is only 67%) and use a linear cavity instead of a ring cavity, because linear cavities are less sensitive than ring cavities to different diffraction angles of the AOM due to different wavelengths. Hence, more optical bandwidth can be achieved with linear cavities.

### 4.4.4 With Semrock filter

One can perform distance measurements with this technique and a smaller optical bandwidth, too, by placing the Semrock filter in the cavity of the FSF laser. But one encounters the same problems as described in Chapter 4.2.3. The reduced optical bandwidth reduces the distance resolution. Judging by Figure 4.17, the $NBW$ would have to be between 10kHz and 100kHz to definitely determine the correct center frequency. A $NBW$ between 10kHz and 100kHz would then correspond to a distance resolution between 65$\mu$m and 646$\mu$m.

[2]The distance difference in our setup was always approximately 30cm. This corresponds to a time difference of approximately 1ns. That means the seed laser drifts less than 20Hz within this 1ns.

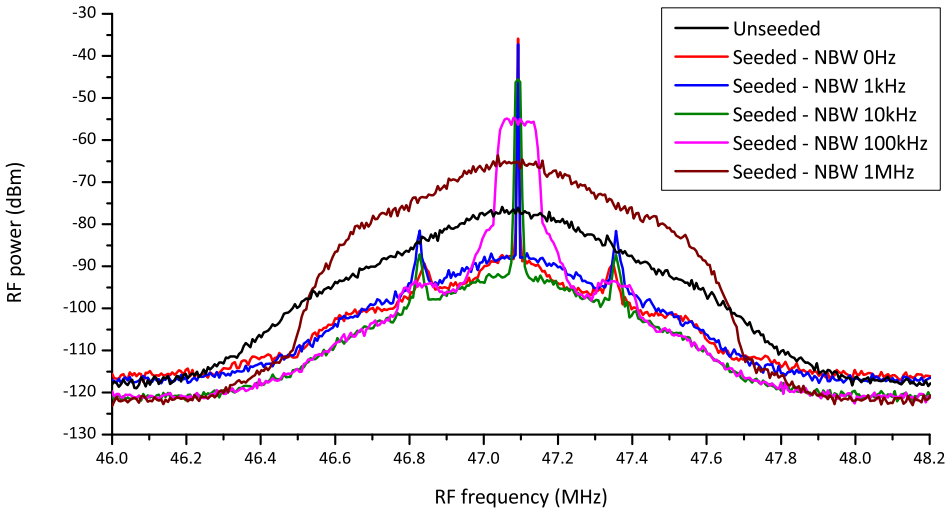


**Figure 4.17.:** A smaller optical bandwidth results in a broader RF beat signal in the unseeded case. The different NBWs shown in this figure are all smaller than the spectral width of the unseeded case.

### 4.4.5 Diffuse target

For the measurements in this Section, the setup of the Michelson interferometer had to contain the lenses again. The target was again a white paper which was put in front of the high reflector.

Figure 4.18 (a) shows the RF beat signals with a modulation frequency smaller than the spectral width. With paper as a target, the light is reflected at different layers of the paper, as described in Section 4.3. This effect coupled with the spectra width due to phase modulation with a specific NBW makes the best choice for the correct center frequency difficult. Hence, a high-accuracy distance measurement is difficult with targets that do not reflect the light at the surface.

The target was placed in front of a mirror, and one can see a section, where the signal is very weak in the middle of the peak in Figure 4.18 (b). It is assumed that this due to the distance between the paper and the mirror. This would mean that one can see the paper target twice in the RF beat spectrum.

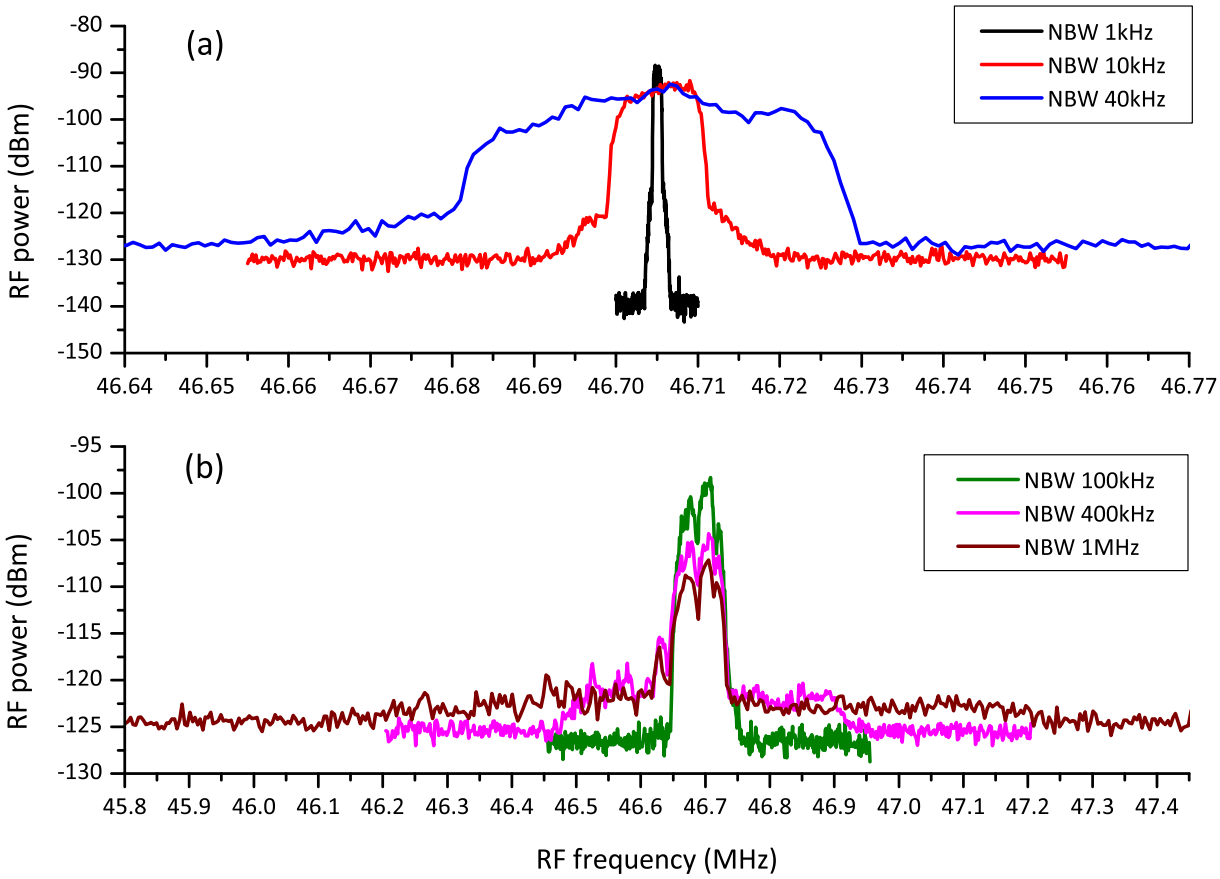


**Figure 4.18.:** RF beat signals for various $NBW$s. When modulating with a larger NBW, one can see how well the different layers of the paper reflect the light.

# 5 Summary

Optical frequency-domain ranging (OFDR) with FSF lasers is an interesting way of doing interferometric distance measurement. If one can resolve all ambiguities, has enough light for detection, and the distance to the target is less than half the coherence length of the light, then it will not matter whether the target is as close as 1m or as far as 1km away from the detector. The distance will be measured with the same accuracy. To calculate the distance from the measured frequencies the *Discrete Frequency Model* [17] proved to be very useful.

In this thesis, seeding the FSF laser with a phase-modulated ultranarrow-linewidth single-frequency laser resulted in an improvement of the SNR of approximately 50dB. With this high SNR, it was possible to demonstrate distance measurement of diffuse targets which was impossible without seeding. But this thesis did not focus on an optical system which allows distance measurement of diffuse targets with multiple pixels simultaneously. This remains a challenge for future research.

The demonstrated precision of the measurement process was 6.5$\mu$m in this thesis. The optical bandwidth was larger than the one required for real-time 3D video, though. According to the calculations in my previous thesis [16], the optical bandwidth would have to be in the order of a $\frac{1}{10}$ of the bandwidth used here. This would result in a precision lower than 100$\mu$m which is still a resolution that one cannot achieve with triangulation or time-of-flight measurement principles at the current state of technology.

The measurements with the pre-set distance resolution, shown in this thesis and [23], gives a new insight in the physics underlying this measurement principle. The resulting beat spectrum is always a mixture of the seed laser spectrum and a pedestal created from the beat of the spontaneous emission light in the FSF laser. Unfortunately, there is the mathematical description of this behavior is yet to be developed. The measurement resolution in this thesis ranges from 6.5$\mu$m up to 646$\mu$m, and in some cases even 6.455mm. This measurement principle offers the choice of an optimum NBW with the highest SNR for a given resolution because none of the seed light is used for a beat signal of a neighboring frequency step. And the principle allows using fewer frequency steps to resolve the ambiguity, too. Both features are very desirable for real-time 3D video. If one has one pixel, one can drastically decrease the measurement duration by adjusting the $NBW$ each measurement and thereby use a successive approximation approach.

To achieve an even better distance resolution, the optical bandwidth has to be increased. One way of doing that is to use a linear cavity instead of a ring cavity because the frequency-dependent diffraction of the AOM limits the bandwidth of the FSF laser and linear cavities are less sensitive to this frequency-dependence. But then one will also need

an AOM with higher diffraction efficiency because the light has to pass the AOM twice. A combination of these measures might push the limits of the distance resolution towards a fraction of the used wavelength [17] and the limit of 129nm imposed by the <20Hz beat linewidth, proposed in [23].

# A Appendix

## A.1 Calculation of the beat frequencies

This appendix presents detailed calculations of the beat frequencies using the discrete frequency model introduced by Yatsenko *et al.* in [21]. Here, $f_{AOM}$ is the AOM frequency and $T_R$ is the cavity round-trip time.
The electric field is defined as

$$E(t) = \sum_{q=0}^{N} E_q(t)\, e^{i\,2\pi\,(f_{seed}+q\,f_{AOM})\,t} = \sum_{q=0}^{N} \varepsilon_{norm}\; a_q\; e^{i\,2\pi\,((f_{seed}+q\,f_{AOM})\,t+\varphi_{seed}(t-q\,T_R)+\theta_q)} \tag{A.1}$$

with the complex amplitude

$$E_q(t) = \varepsilon_{norm}\; a_q\; e^{i\,2\pi\,(\varphi_{seed}(t-q\,T_R)+\theta_q)} \tag{A.2}$$

where $f_{seed}$ is the (optical) frequency of the seed laser, $f_{AOM}$ is the AOM frequency, $\varphi_{seed}$ is a variable part of the phase, $\theta_q$ is the fixed part of the phase, and $N$ is the number of modes in the cavity. $\varepsilon_{norm}$ stands for a normalization factor and $a_q$ for the amplitude of the mode $q$. This together forms a frequency comb starting at the frequency $f_{seed}$. The comb lines are separated by $f_{AOM}$ and there are $N+1$ lines.
As an ansatz for the constant phase of each mode, we use

$$\theta_q = T_R\, q \left( f_{seed} + (q+1)\;\frac{f_{AOM}}{2} \right) + \theta_0 \tag{A.3}$$

where $\theta_0$ is a constant. Due to the optical frequency $f_{seed}$, there is a phase shift after each round trip $T_R\, f_{seed}$. Additionally, there is a phase shift due to the AOM frequency which increases the frequency after each round trip. After one round trip, the phase shift is $T_R\, f_{AOM}$, after two it is $T_R\, f_{AOM} + 2\,T_R\, f_{AOM}$, after three it is $T_R\, f_{AOM} + 2\,T_R\, f_{AOM} + 3\,T_R\, f_{AOM}$, and so on. A general formula for this is $\frac{q(q+1)}{2}\, T_R\, f_{AOM}$.
A useful equation will be

$$\theta_{q+p} - \theta_q = T_R \left( p\, f_{seed} + \left(p^2 + p + 2qp\right)\;\frac{f_{AOM}}{2} \right) \quad . \tag{A.4}$$

The intensity is defined as

$$I\,(t) = \frac{n c_0 \epsilon_0}{2}\,|E\,(t)|^2 \quad . \tag{A.5}$$

### A.1.1 Michelson interferometer

The intensity after the Michelson interferometer can be obtained as follows

$$I(t) \propto \left|\delta\, E(t) + \eta\, E\left(t - \frac{2L}{c_0}\right) e^{i\,2\pi\,\Delta\phi}\right|^2 = \delta^2 \left|E(t)\right|^2 + \eta^2 \left|E\left(t - \frac{2L}{c_0}\right)\right|^2 + \delta\eta \left|E^*(t)\;\; E\left(t - \frac{2L}{c_0}\right) e^{i\,2\pi\,\Delta\phi} + E(t)\;\; E^*\left(t - \frac{2L}{c_0}\right) e^{-i\,2\pi\,\Delta\phi}\right| \tag{A.6}$$

$$I(t) \propto I_1(t) + I_2(t) + I_3(t) \tag{A.7}$$

$$I_1(t) = \delta^2 \left|E(t)\right|^2 \tag{A.8}$$

$$I_2(t) = \eta^2 \left|E\left(t - \frac{2L}{c_0}\right)\right|^2 \tag{A.9}$$

$$I_3(t) = \delta\eta \left|E^*(t)\;\; E\left(t - \frac{2L}{c_0}\right) e^{i\,2\pi\,\Delta\phi} + E(t)\;\; E^*\left(t - \frac{2L}{c_0}\right) e^{-i\,2\pi\,\Delta\phi}\right| \tag{A.10}$$

$\delta$ and $\eta$ represent the dampings in the two arms, and $\Delta\phi$ represents the phase shift difference between the two targets due to different target materials. The intensity can be split in three terms. $I_1(t)$ and $I_2(t)$ correspond to autocorrelations of the light from the individual arms. $I_3(t)$ is a correlation term of the two arms and it will yield the distance dependence.

In the following calculation, we will always encounter products of sums. I solved a similar problem in my first diploma thesis [16] and we will use the same pattern here.

Since there are only discrete frequencies present, the result will only contain discrete beat frequencies. We can define a beat index $p$. It states which terms, peaks of the frequency comb, have to be multiplied with which other terms. If $p = 0$, only terms with the same index (of the same frequency peak) will be multiplied. If $p = 1$, only terms with a difference of one in their index will be multiplied (that means a multiplication with neighboring peaks), and so on. This scheme can be seen in Table A.1.

| | | | | | | | | | | | | | | |
|---|---|---|---|---|---|---|---|---|---|---|---|---|---|---|
| ⋮ | | | | ⋮ | | ⋮ | | | ⋮ | ⋮ | | | | ⋮ |
| | | | | | | | ↗ | | | | | | ↗ | |
| $\mathcal{E}_3$ | ← | $p=0$ | → | $\mathcal{E}_3$ | | $\mathcal{E}_3$ | ← | $p=1$ | $\mathcal{E}_3$ | $\mathcal{E}_3$ | | $p=2$ | | $\mathcal{E}_3$ |
| | | | | | | | ↗ | | | | ↙ | | ↗ | |
| $\mathcal{E}_2$ | ← | $p=0$ | → | $\mathcal{E}_2$ | | $\mathcal{E}_2$ | ← | $p=1$ | $\mathcal{E}_2$ | $\mathcal{E}_2$ | | $p=2$ | | $\mathcal{E}_2$ |
| | | | | | | | ↗ | | | | ↙ | | | |
| $\mathcal{E}_1$ | ← | $p=0$ | → | $\mathcal{E}_1$ | | $\mathcal{E}_1$ | ← | $p=1$ | $\mathcal{E}_1$ | $\mathcal{E}_1$ | | | | $\mathcal{E}_1$ |

**Table A.1.:** Pattern for calculating the product of a sum with a sum

with

$$\mathcal{E}_q = E_q(t)\, e^{i\,2\pi\,(f_{seed} + q\, f_{AOM})\, t} \quad . \tag{A.11}$$

#### *A.1.1.1 Autocorrelation terms*

If we apply this pattern to the autocorrelation terms, we obtain

$$\begin{aligned}
I_1(t) &= \delta^2 \left|E\left(t\right)\right|^2 = \delta^2 \left(\sum_{q=1}^{N} E_q\left(t\right)\ e^{i\,2\pi\left(f_{seed}+q\,f_{AOM}\right)t}\right)\left(\sum_{q=1}^{N} E_q^*\left(t\right)\ e^{-i\,2\pi\left(f_{seed}+q\,f_{AOM}\right)t}\right) \\
&= \delta^2 \sum_{p=0}^{N} \frac{1}{2}\left(E_0\left(t\right)\ E_p^*\left(t\right)\ e^{-i\,2\pi\,p\,f_{AOM}\,t} + \cdots + E_{N-p}\left(t\right)\ E_N^*\left(t\right)\ e^{-i\,2\pi\,p\,f_{AOM}\,t}\right. \\
&\quad \left. + E_p\left(t\right)\ E_0^*\left(t\right)\ e^{i\,2\pi\,p\,f_{AOM}\,t} + \cdots + E_N\left(t\right)\ E_{N-p}^*\left(t\right)\ e^{i\,2\pi\,p\,f_{AOM}\,t}\right) \\
&= \delta^2 \sum_{p=0}^{N}\sum_{q=0}^{N-p} \frac{\left|\varepsilon_{norm}\right|^2 a_q\ a_{q+p}}{2}\left(e^{-i\,2\pi\left(q\,f_{AOM}\,t+\varphi_{seed}(t-(q+p)\,T_R)-\varphi_{seed}(t-q\,T_R)+\theta_{q+p}-\theta_q\right)}\right. \\
&\quad \left. + e^{i\,2\pi\left(q\,f_{AOM}\,t+\varphi_{seed}(t-(q+p)\,T_R)-\varphi_{seed}(t-q\,T_R)+\theta_{q+p}-\theta_q\right)}\right) \\
&= \delta^2 \sum_{p=0}^{N}\sum_{q=0}^{N-p} \left|\varepsilon_{norm}\right|^2 a_q\ a_{q+p}\ \cos\left(2\pi\left(p\,f_{AOM}\,t+\varphi_{seed}\left(t-(q+p)\,T_R\right)\right.\right. \\
&\quad \left.\left. - \varphi_{seed}\left(t-q\,T_R\right) + T_R\left(p\,f_{seed} + \left(p^2+p+2qp\right)\ \frac{f_{AOM}}{2}\right)\right)\right)
\end{aligned} \tag{A.12}$$

$$\begin{aligned}
I_2(t) &= \eta^2 \left|E\left(t-\frac{2L}{c_0}\right)\right|^2 \\
&= \eta^2 \sum_{p=0}^{N}\sum_{q=0}^{N-p} \left|\varepsilon_{norm}\right|^2 a_q\ a_{q+p}\ \cos\left(2\pi\left(p\,f_{AOM}\,t+\varphi_{seed}\left(t-\frac{2L}{c_0}-(q+p)\,T_R\right)\right.\right. \\
&\quad \left.\left. - \varphi_{seed}\left(t-\frac{2L}{c_0}-q\,T_R\right) - p\,f_{AOM}\,\frac{2L}{c_0} + T_R\left(p\,f_{seed}+\left(p^2+p+2qp\right)\ \frac{f_{AOM}}{2}\right)\right)\right)
\end{aligned} \tag{A.13}$$

#### *A.1.1.2 Terms with a distance dependence*

The terms with a distance dependence can be calculated with the same pattern. Therefore,

$$\begin{aligned}
I_3(t) &= \delta\eta \left|E^*\left(t\right)\ E\left(t-\frac{2L}{c_0}\right)\ e^{i\,2\pi\,\Delta\phi} + E\left(t\right)\ E^*\left(t-\frac{2L}{c_0}\right)\ e^{-i\,2\pi\,\Delta\phi}\right| \\
&= \delta\eta \sum_{p=0}^{N}\sum_{q=0}^{N-p} \frac{\left|\varepsilon_{norm}\right|^2 a_q\ a_{q+p}}{2}\ e^{-i\,2\pi\left(\left(f_{seed}+q\,f_{AOM}\right)t+\varphi_{seed}(t-q\,T_R)+\theta_q\right)} \\
&\quad \cdot e^{i\,2\pi\left(\left(f_{seed}+(q+p)\,f_{AOM}\right)\left(t-\frac{2L}{c_0}\right)+\varphi_{seed}\left(\left(t-\frac{2L}{c_0}\right)-(q+p)\,T_R\right)+\theta_{q+p}\right)} + c.c. \\
&\quad + e^{i\,2\pi\left(\left(f_{seed}+(q+p)\,f_{AOM}\right)t+\varphi_{seed}(t-(q+p)\,T_R)+\theta_{q+p}\right)} \\
&\quad \cdot e^{-i\,2\pi\left(\left(f_{seed}+q\,f_{AOM}\right)\left(t-\frac{2L}{c_0}\right)+\varphi_{seed}\left(\left(t-\frac{2L}{c_0}\right)-q\,T_R\right)+\theta_q\right)} + c.c.
\end{aligned}$$

$$
\begin{aligned}
I_3(t) = \delta\eta \sum_{p=0}^{N} \sum_{q=0}^{N-p} \frac{\left|\varepsilon_{norm}\right|^2 a_q\, a_{q+p}}{2} \Bigg( & e^{i\,2\pi \left(p\, f_{AOM}\, t - (f_{seed}+(q+p)f_{AOM})\, \frac{2L}{c_0} + \varphi_{seed}\left(t - \frac{2L}{c_0} - (q+p)\, T_R\right)\right)} \\
& \cdot e^{i\,2\pi\,(-\varphi_{seed}(t - q\,T_R) + \theta_{q+p} - \theta_q + \Delta\phi)} + c.c. + e^{i\,2\pi \left(p\, f_{AOM}\, t + (f_{seed}+(q+p)f_{AOM})\, \frac{2L}{c_0}\right)} \\
& \cdot e^{i\,2\pi \left(\varphi_{seed}(t - (q+p)\, T_R) - \varphi_{seed}\left(t - \frac{2L}{c_0} - q\, T_R\right) + \theta_{q+p} - \theta_q - \Delta\phi\right)} + c.c. \Bigg) \\
= \delta\eta \sum_{p=0}^{N} \sum_{q=0}^{N-p} & \left|\varepsilon_{norm}\right|^2 a_q\, a_{q+p} \\
& \cdot \Bigg( \cos\Bigg( 2\pi \Bigg( p\, f_{AOM}\, t + \varphi_{seed}\left(t - \frac{2L}{c_0} - (q+p)\, T_R\right) - \varphi_{seed}\,(t - qT_R) \\
& - \left(f_{seed} + (q+p)\, f_{AOM}\right) \frac{2L}{c_0} + T_R \left( p\, f_{seed} + \left(p^2 + p + 2qp\right) \frac{f_{AOM}}{2}\right) + \Delta\phi \Bigg)\Bigg) \\
& + \cos\Bigg( 2\pi \Bigg( p\, f_{AOM}\, t + \varphi_{seed}\,(t - (q+p)\, T_R) - \varphi_{seed}\left(t - \frac{2L}{c_0} - qT_R\right) \\
& + \left(f_{seed} + (q+p)\, f_{AOM}\right) \frac{2L}{c_0} + T_R \left( p\, f_{seed} + \left(p^2 + p + 2qp\right) \frac{f_{AOM}}{2}\right) - \Delta\phi \Bigg)\Bigg)\Bigg)
\end{aligned}
\tag{A.14}
$$

### *A.1.1.3 Substitutions*

In order to make the equations easier to write, we define the following substitutions:

$$\varphi_{seed,q} = \varphi_{seed}\,(t - qT_R) \tag{A.15}$$

$$\varphi_{seed,qp} = \varphi_{seed}\,(t - (q+p)\, T_R) \tag{A.16}$$

$$\varphi_{seed,qL} = \varphi_{seed}\left(t - \frac{2L}{c_0} - qT_R\right) \tag{A.17}$$

$$\varphi_{seed,qpL} = \varphi_{seed}\left(t - \frac{2L}{c_0} - (q+p)\, T_R\right) \tag{A.18}$$

$$\xi_1 = \theta_{q+p} - \theta_q = T_R \left( p\, f_{seed} + \left(p^2 + p + 2qp\right) \frac{f_{AOM}}{2}\right) \tag{A.19}$$

$$\xi_2 = -p\, f_{AOM}\, \frac{2L}{c_0} \tag{A.20}$$

$$\xi_3 = \left(f_{seed} + (q+p)\, f_{AOM}\right) \frac{2L}{c_0} - \Delta\phi \tag{A.21}$$

Hence,

$$I_1(t) = \delta^2 \sum_{p=0}^{N} \sum_{q=0}^{N-p} |\varepsilon_{norm}|^2 \, a_q \, a_{q+p} \, \cos\left(2\pi \left(p \, f_{AOM} \, t + \varphi_{seed,qp} - \varphi_{seed,q} + \xi_1\right)\right) \tag{A.22}$$

$$I_2(t) = \eta^2 \sum_{p=0}^{N} \sum_{q=0}^{N-p} |\varepsilon_{norm}|^2 \, a_q \, a_{q+p} \, \cos\left(2\pi \left(p \, f_{AOM} \, t + \varphi_{seed,qpL} - \varphi_{seed,qL} + \xi_1 + \xi_2\right)\right) \tag{A.23}$$

$$\begin{aligned} I_3(t) = \delta\eta \sum_{p=0}^{N} \sum_{q=0}^{N-p} |\varepsilon_{norm}|^2 \, a_q \, a_{q+p} \, \Big(&\cos\left(2\pi \left(p \, f_{AOM} \, t + \varphi_{seed,qpL} - \varphi_{seed,q} + \xi_1 - \xi_3\right)\right) \\ &+ \cos\left(2\pi \left(p \, f_{AOM} \, t + \varphi_{seed,qp} - \varphi_{seed,qL} + \xi_1 + \xi_3\right)\right)\Big) \end{aligned} \tag{A.24}$$

### A.1.2 Sinusoidal phase modulation

We want to perform phase modulation of the seed laser with an EOM. Hence,

$$\varphi_{seed}(t) = \varphi_0 + A_{EOM} \, \sin\left(2\pi \, f_{EOM} \, t\right) \tag{A.25}$$

where $\varphi_0$ is a constant phase offset due to the EOM crystal. The second term represents a phase modulation with a sine of frequency $f_{EOM}$ and amplitude $A_{EOM}$.

With the trigonometric identity $\sin(\alpha) - \sin(\beta) = 2\sin\left(\frac{\alpha-\beta}{2}\right)\cos\left(\frac{\alpha+\beta}{2}\right)$, we obtain for the $\varphi_{seed}$ terms:

$$\begin{aligned} &\varphi_{seed,qp} - \varphi_{seed,q} = \\ &\quad = -2A_{EOM} \, \sin\left(2\pi \, f_{EOM} \, \frac{p}{2} T_R\right) \cos\left(2\pi \, f_{EOM} \, \left(t - \left(q + \frac{p}{2}\right) T_R\right)\right) \end{aligned} \tag{A.26}$$

$$\begin{aligned} &\varphi_{seed,qpL} - \varphi_{seed,qL} = \\ &\quad = -2A_{EOM} \, \sin\left(2\pi \, f_{EOM} \, \frac{p}{2} T_R\right) \cos\left(2\pi \, f_{EOM} \, \left(t - \frac{2L}{c_0} - \left(q + \frac{p}{2}\right) T_R\right)\right) \end{aligned} \tag{A.27}$$

$$\begin{aligned} &\varphi_{seed,qpL} - \varphi_{seed,q} = \\ &\quad = -2A_{EOM} \, \sin\left(2\pi \, f_{EOM} \, \left(\frac{L}{c_0} + \frac{p}{2} T_R\right)\right) \cos\left(2\pi \, f_{EOM} \, \left(t - \frac{L}{c_0} - \left(q + \frac{p}{2}\right) T_R\right)\right) \end{aligned} \tag{A.28}$$

$$\begin{aligned} &\varphi_{seed,qp} - \varphi_{seed,qL} = \\ &\quad = -2A_{EOM} \, \sin\left(2\pi \, f_{EOM} \, \left(-\frac{L}{c_0} + \frac{p}{2} T_R\right)\right) \cos\left(2\pi \, f_{EOM} \, \left(t + \frac{L}{c_0} - \left(q + \frac{p}{2}\right) T_R\right)\right) \end{aligned} \tag{A.29}$$

With the substitutions

$$A = -2A_{EOM} \tag{A.30}$$

$$\psi_p = 2\pi\, f_{EOM}\, \frac{p}{2} T_R \tag{A.31}$$

$$\psi_{p,L} = 2\pi\, f_{EOM}\, \left(\frac{L}{c_0} + \frac{p}{2} T_R\right) \tag{A.32}$$

$$\psi_{p,-L} = 2\pi\, f_{EOM}\, \left(-\frac{L}{c_0} + \frac{p}{2} T_R\right) \tag{A.33}$$

$$\rho_0 = 2\pi\, f_{EOM}\, \left(t - \left(q + \frac{p}{2}\right) T_R\right) \tag{A.34}$$

$$\rho_{-L} = 2\pi\, f_{EOM}\, \left(t - \frac{L}{c_0} - \left(q + \frac{p}{2}\right) T_R\right) \tag{A.35}$$

$$\rho_{L} = 2\pi\, f_{EOM}\, \left(t + \frac{L}{c_0} - \left(q + \frac{p}{2}\right) T_R\right) \tag{A.36}$$

$$\rho_{-2L} = 2\pi\, f_{EOM}\, \left(t - \frac{2L}{c_0} - \left(q + \frac{p}{2}\right) T_R\right) \quad , \tag{A.37}$$

we get

$$\varphi_{seed,qp} - \varphi_{seed,q} = A \sin\left(\psi_p\right) \cos\left(\rho_0\right) \tag{A.38}$$

$$\varphi_{seed,qpL} - \varphi_{seed,q} = A \sin\left(\psi_{p,L}\right) \cos\left(\rho_{-L}\right) \tag{A.39}$$

$$\varphi_{seed,qp} - \varphi_{seed,qL} = A \sin\left(\psi_{p,-L}\right) \cos\left(\rho_{L}\right) \tag{A.40}$$

$$\varphi_{seed,qpL} - \varphi_{seed,qL} = A \sin\left(\psi_{p}\right) \cos\left(\rho_{-2L}\right) \quad . \tag{A.41}$$

In order to get simpler results, we need the Bessel functions $J_n$ with the identity

$$e^{iB\cos\chi} = \sum_{n=-\infty}^{\infty} i^n J_n\left(B\right) e^{in\chi} \quad . \tag{A.42}$$

In the Eqs. (A.22 - A.24, A.38 - A.41), we can see that there are always terms of the form $\cos\left(\phi + B\cos\chi\right)$. Hence,

$$\begin{aligned}
\cos\left(\phi + B\cos\chi\right) &= \frac{e^{i(\phi + B\cos\chi)} + e^{-i(\phi + B\cos(-\chi))}}{2} \\
&= \frac{1}{2}\left(e^{i\phi} \sum_{n=-\infty}^{\infty} i^n J_n(B) e^{in\chi} + e^{-i\phi} \sum_{n=-\infty}^{\infty} i^n J_n(B) e^{-in\chi}\right) \\
&= \frac{1}{2} \sum_{n=-\infty}^{\infty} i^n \left(J_n(B) e^{i(\phi + n\chi)} + J_n(-B) e^{-i(\phi + n\chi)}\right) \\
&= \sum_{n=-\infty}^{\infty} i^{2n} \left(\frac{J_{2n}(B) e^{i(\phi + 2n\chi)} + J_{2n}(B) e^{-i(\phi + 2n\chi)}}{2}\right. \\
&\qquad \left. + \frac{J_{2n-1}(B) e^{i(\phi + (2n-1)\chi)} - J_{2n-1}(B) e^{-i(\phi + (2n-1)\chi)}}{2i}\right) \\
&= \sum_{n=-\infty}^{\infty} (-1)^n \left(J_{2n}(B) \cos\left(\phi + 2n\chi\right) + J_{2n-1}(B) \sin\left(\phi + (2n-1)\,\chi\right)\right)
\end{aligned} \tag{A.43}$$

Now, we can use this result to calculate the first intensity term.

$$
\begin{aligned}
I_1(t) &= \delta^2 \sum_{p=0}^{N} \sum_{q=0}^{N-p} |\varepsilon_{norm}|^2 \, a_q \, a_{q+p} \; \cos\left(2\pi \left(p \, f_{AOM} \, t + \varphi_{seed,qp} - \varphi_{seed,q} + \xi_1\right)\right) \\
&= \delta^2 \sum_{p=0}^{N} \sum_{q=0}^{N-p} |\varepsilon_{norm}|^2 \, a_q \, a_{q+p} \; \cos\left(2\pi \left(p \, f_{AOM} \, t + \xi_1\right) - 4\pi \, A_{EOM} \sin\left(\psi_p\right) \cos\left(\rho_0\right)\right) \\
&= \delta^2 \sum_{p=0}^{N} \sum_{q=0}^{N-p} \sum_{n=-\infty}^{\infty} (-1)^n \, |\varepsilon_{norm}|^2 \, a_q \, a_{q+p} \\
&\quad \cdot \left(J_{2n}\left(4\pi \, A_{EOM} \sin\left(\psi_p\right)\right) \; \cos\left(2\pi \left(p \, f_{AOM} \, t + \xi_1\right) + 2n\rho_0\right)\right. \\
&\quad \left. + \; J_{2n-1}\left(4\pi \, A_{EOM} \sin\left(\psi_p\right)\right) \; \sin\left(2\pi \left(p \, f_{AOM} \, t + \xi_1\right) + \left(2n-1\right)\rho_0\right)\right) \qquad \text{(A.44)} \\
&= \delta^2 \sum_{p=0}^{N} \sum_{q=0}^{N-p} \sum_{n=-\infty}^{\infty} (-1)^n \, |\varepsilon_{norm}|^2 \, a_q \, a_{q+p} \\
&\quad \cdot \left(J_{2n}\left(4\pi \, A_{EOM} \sin\left(\pi \, p \, f_{EOM} T_R\right)\right) \; \cos\left(2\pi \left(\left(p f_{AOM} + 2n f_{EOM}\right) t\right.\right.\right. \\
&\quad \left.\left.\left. + \; T_R \left(p \, f_{seed} + \left(p^2 + p + 2qp\right) \; \frac{f_{AOM}}{2} - n \left(2q + p\right) f_{EOM}\right)\right)\right)\right. \\
&\quad \left. + J_{2n-1}\left(4\pi \, A_{EOM} \sin\left(\pi \, p \, f_{EOM} T_R\right)\right) \; \sin\left(2\pi \left(\left(p f_{AOM} + \left(2n-1\right) f_{EOM}\right) t\right.\right.\right. \\
&\quad \left.\left.\left. + \; T_R \left(p \, f_{seed} + \left(p^2 + p + 2qp\right) \; \frac{f_{AOM}}{2} - \left(2n-1\right) \left(q + \frac{p}{2}\right) f_{EOM}\right)\right)\right)\right) \qquad \text{(A.45)} \\
&= \delta^2 \sum_{p=0}^{N} \sum_{q=0}^{N-p} \sum_{n=-\infty}^{\infty} (-1)^n \, |\varepsilon_{norm}|^2 \, a_q \, a_{q+p} \left(J_{2n}\left(M_1\right) \cos\left(2\pi \left(f_{even} \, t + \varphi_{1,even}\right)\right)\right. \\
&\quad \left. + \; J_{2n-1}\left(M_1\right) \sin\left(2\pi \left(f_{odd} \, t + \varphi_{1,odd}\right)\right)\right) \qquad \text{(A.46)}
\end{aligned}
$$

where

$$
\begin{aligned}
M_1 &= 4\pi \, A_{EOM} \sin\left(\pi \, p \, f_{EOM} T_R\right) && \text{(A.47)} \\
f_{odd} &= p \, f_{AOM} + \left(2n-1\right) f_{EOM} && \text{(A.48)} \\
f_{even} &= p \, f_{AOM} + 2n f_{EOM} && \text{(A.49)} \\
\varphi_{1,odd} &= T_R \left(p \, f_{seed} + \left(p^2 + p + 2qp\right) \; \frac{f_{AOM}}{2} - \left(2n-1\right) \left(q + \frac{p}{2}\right) f_{EOM}\right) && \text{(A.50)} \\
\varphi_{1,even} &= T_R \left(p \, f_{seed} + \left(p^2 + p + 2qp\right) \; \frac{f_{AOM}}{2} - n \left(2q + p\right) f_{EOM}\right) && \text{(A.51)}
\end{aligned}
$$

The second term can be evaluated with the same scheme.

$$
\begin{aligned}
I_2(t) &= \eta^2 \sum_{p=0}^{N} \sum_{q=0}^{N-p} \left|\varepsilon_{norm}\right|^2 a_q \, a_{q+p} \, \cos\left(2\pi \left(p \, f_{AOM} \, t + \varphi_{seed,qpL} - \varphi_{seed,qL} + \xi_1 + \xi_2\right)\right) \\
&= \eta^2 \sum_{p=0}^{N} \sum_{q=0}^{N-p} \sum_{n=-\infty}^{\infty} (-1)^n \left|\varepsilon_{norm}\right|^2 a_q \, a_{q+p} \\
&\quad \cdot \left(J_{2n}\left(4\pi \, A_{EOM} \sin\left(\psi_p\right)\right) \, \cos\left(2\pi \left(p \, f_{AOM} \, t + \xi_1 + \xi_2\right) + 2n \, \rho_{-2L}\right)\right. \\
&\quad \left. + \, J_{2n-1}\left(4\pi \, A_{EOM} \sin\left(\psi_p\right)\right) \, \sin\left(2\pi \left(p \, f_{AOM} \, t + \xi_1 + \xi_2\right) + \left(2n-1\right) \rho_{-2L}\right)\right) \\
&= \eta^2 \sum_{p=0}^{N} \sum_{q=0}^{N-p} \sum_{n=-\infty}^{\infty} (-1)^n \left|\varepsilon_{norm}\right|^2 a_q \, a_{q+p} \left(J_{2n}\left(4\pi \, A_{EOM} \sin\left(\pi \, p \, f_{EOM} T_R\right)\right)\right. \\
&\quad \cdot \cos\left(2\pi \left(\left(p f_{AOM} + 2n f_{EOM}\right) t + T_R \left(p \, f_{seed} + \left(p^2 + p + 2qp\right) \, \frac{f_{AOM}}{2}\right.\right.\right. \\
&\quad \left.\left.\left. - \, n \left(2q + p\right) f_{EOM}\right) - \left(p \, f_{AOM} + 2n f_{EOM}\right) \frac{2L}{c_0}\right)\right) \\
&\quad + J_{2n-1}\left(4\pi \, A_{EOM} \sin\left(\pi \, p \, f_{EOM} T_R\right)\right) \, \sin\left(2\pi \left(\left(p f_{AOM} + \left(2n-1\right) f_{EOM}\right) t\right.\right. \\
&\quad \left. + T_R \left(p \, f_{seed} + \left(p^2 + p + 2qp\right) \, \frac{f_{AOM}}{2} - \left(2n-1\right) \left(q + \frac{p}{2}\right) f_{EOM}\right)\right. \\
&\quad \left.\left. - \, \left(p \, f_{AOM} + \left(2n-1\right) f_{EOM}\right) \frac{2L}{c_0}\right)\right)\right) \qquad \text{(A.52)} \\
&= \eta^2 \sum_{p=0}^{N} \sum_{q=0}^{N-p} \sum_{n=-\infty}^{\infty} (-1)^n \left|\varepsilon_{norm}\right|^2 a_q \, a_{q+p} \left(J_{2n}\left(M_1\right) \cos\left(2\pi \left(f_{even} \, t + \varphi_{2,even}\right)\right)\right. \\
&\quad \left. + \, J_{2n-1}\left(M_1\right) \sin\left(2\pi \left(f_{odd} \, t + \varphi_{2,odd}\right)\right)\right) \qquad \text{(A.53)}
\end{aligned}
$$

where

$$
\begin{aligned}
\varphi_{2,odd} &= T_R \left(p \, f_{seed} + \left(p^2 + p + 2qp\right) \, \frac{f_{AOM}}{2} - \left(2n-1\right) \left(q + \frac{p}{2}\right) f_{EOM}\right) \\
&\quad - \left(p \, f_{AOM} + \left(2n-1\right) f_{EOM}\right) \frac{2L}{c_0} \qquad \text{(A.54)} \\
\varphi_{2,even} &= T_R \left(p \, f_{seed} + \left(p^2 + p + 2qp\right) \, \frac{f_{AOM}}{2} - n \left(2q + p\right) f_{EOM}\right) \\
&\quad - \left(p \, f_{AOM} + 2n f_{EOM}\right) \frac{2L}{c_0} \qquad \text{(A.55)}
\end{aligned}
$$

The mixed term can be calculated as

$$
\begin{aligned}
I_3(t) = \delta\eta \sum_{p=0}^{N} \sum_{q=0}^{N-p} |\varepsilon_{norm}|^2 \, a_q \, a_{q+p} \;\; & (\cos\left(2\pi \left(p\, f_{AOM}\, t + \varphi_{seed,qpL} - \varphi_{seed,q} + \xi_1 - \xi_3\right)\right) \\
& + \cos\left(2\pi \left(p\, f_{AOM}\, t + \varphi_{seed,qp} - \varphi_{seed,qL} + \xi_1 + \xi_3\right)\right)) \\
= \delta\eta \sum_{p=0}^{N} \sum_{q=0}^{N-p} \sum_{n=-\infty}^{\infty} & (-1)^n \, |\varepsilon_{norm}|^2 \, a_q \, a_{q+p} \\
& \cdot \left(J_{2n}\left(4\pi\, A_{EOM} \sin\left(\psi_{p,L}\right)\right) \, \cos\left(2\pi \left(p\, f_{AOM}\, t + \xi_1 - \xi_3\right) + 2n\, \rho_{-L}\right)\right. \\
& + J_{2n-1}\left(4\pi\, A_{EOM} \sin\left(\psi_{p,L}\right)\right) \, \sin\left(2\pi \left(p\, f_{AOM}\, t + \xi_1 - \xi_3\right) + (2n-1)\, \rho_{-L}\right) \\
& + J_{2n}\left(4\pi\, A_{EOM} \sin\left(\psi_{p,-L}\right)\right) \, \cos\left(2\pi \left(p\, f_{AOM}\, t + \xi_1 + \xi_3\right) + 2n\, \rho_{L}\right) \\
& \left. + \, J_{2n-1}\left(4\pi\, A_{EOM} \sin\left(\psi_{p,-L}\right)\right) \, \sin\left(2\pi \left(p\, f_{AOM}\, t + \xi_1 + \xi_3\right) + (2n-1)\, \rho_{L}\right)\right)
\end{aligned}
\tag{A.56}
$$

$$
\begin{aligned}
= \delta\eta \sum_{p=0}^{N} \sum_{q=0}^{N-p} \sum_{n=-\infty}^{\infty} & (-1)^n \, |\varepsilon_{norm}|^2 \, a_q \, a_{q+p} \\
& \cdot \left( J_{2n}\left(4\pi\, A_{EOM} \sin\left(2\pi\, f_{EOM}\, \left(\frac{L}{c_0} + \frac{p}{2} T_R\right)\right)\right)\right. \\
& \quad \cdot \cos\left(2\pi \left( \left(p f_{AOM} + 2n f_{EOM}\right) t - \left(f_{seed} + (q+p)\, f_{AOM} - n\, f_{EOM}\right) \frac{2L}{c_0}\right.\right. \\
& \qquad \left.\left. + \, T_R \left(p\, f_{seed} + \left(p^2 + p + 2qp\right) \, \frac{f_{AOM}}{2} - n\,(2q+p)\, f_{EOM}\right) + \, \Delta\phi\right)\right) \\
& + J_{2n-1}\left(4\pi\, A_{EOM} \sin\left(2\pi\, f_{EOM}\, \left(\frac{L}{c_0} + \frac{p}{2} T_R\right)\right)\right) \\
& \quad \cdot \sin\left(2\pi \left( \left(p f_{AOM} + (2n-1)\, f_{EOM}\right) t - \left(f_{seed} + (q+p)\, f_{AOM} - \frac{2n-1}{2}\, f_{EOM}\right) \frac{2L}{c_0}\right.\right. \\
& \qquad \left.\left. + \, T_R \left(p\, f_{seed} + \left(p^2 + p + 2qp\right) \, \frac{f_{AOM}}{2} - (2n-1)\left(q + \frac{p}{2}\right) f_{EOM}\right) + \, \Delta\phi\right)\right) \\
& + J_{2n}\left(4\pi\, A_{EOM} \sin\left(2\pi\, f_{EOM}\, \left(-\frac{L}{c_0} + \frac{p}{2} T_R\right)\right)\right) \\
& \quad \cdot \cos\left(2\pi \left( \left(p f_{AOM} + 2n f_{EOM}\right) t + \left(f_{seed} + (q+p)\, f_{AOM} + n\, f_{EOM}\right) \frac{2L}{c_0}\right.\right. \\
& \qquad \left.\left. + \, T_R \left(p\, f_{seed} + \left(p^2 + p + 2qp\right) \, \frac{f_{AOM}}{2} - n\,(2q+p)\, f_{EOM}\right) - \, \Delta\phi\right)\right) \\
& + J_{2n-1}\left(4\pi\, A_{EOM} \sin\left(2\pi\, f_{EOM}\, \left(-\frac{L}{c_0} + \frac{p}{2} T_R\right)\right)\right) \\
& \quad \cdot \sin\left(2\pi \left( \left(p f_{AOM} + (2n-1)\, f_{EOM}\right) t + \left(f_{seed} + (q+p)\, f_{AOM} + \frac{2n-1}{2}\, f_{EOM}\right) \frac{2L}{c_0}\right.\right. \\
& \qquad \left.\left.\left. + \, T_R \left(p\, f_{seed} + \left(p^2 + p + 2qp\right) \, \frac{f_{AOM}}{2} - (2n-1)\left(q + \frac{p}{2}\right) f_{EOM}\right) - \, \Delta\phi\right)\right)\right)
\end{aligned}
\tag{A.57}
$$

$$I_3(t) = \delta\eta \sum_{p=0}^{N} \sum_{q=0}^{N-p} \sum_{n=-\infty}^{\infty} (-1)^n \left|\varepsilon_{norm}\right|^2 a_q \, a_{q+p} \left( J_{2n}\left(M_{3a}\right) \cos\left(2\pi \left(f_{even}\, t + \varphi_{3a,even}\right)\right) \right.$$
$$+ J_{2n-1}\left(M_{3a}\right) \sin\left(2\pi \left(f_{odd}\, t + \varphi_{3a,odd}\right)\right) + J_{2n}\left(M_{3b}\right) \cos\left(2\pi \left(f_{even}\, t + \varphi_{3b,even}\right)\right)$$
$$\left. + J_{2n-1}\left(M_{3b}\right) \sin\left(2\pi \left(f_{odd}\, t + \varphi_{3b,odd}\right)\right)\right) \tag{A.58}$$

where

$$M_{3a} = 4\pi \, A_{EOM} \sin\left(2\pi \, f_{EOM} \, \left(\frac{L}{c_0} + \frac{p}{2} T_R\right)\right) \tag{A.59}$$

$$M_{3b} = 4\pi \, A_{EOM} \sin\left(2\pi \, f_{EOM} \, \left(-\frac{L}{c_0} + \frac{p}{2} T_R\right)\right) \tag{A.60}$$

$$\varphi_{3a,odd} = T_R \left( p \, f_{seed} + \left(p^2 + p + 2qp\right) \, \frac{f_{AOM}}{2} - (2n-1) \left(q + \frac{p}{2}\right) f_{EOM} \right)$$
$$- \left( f_{seed} + (q+p) \, f_{AOM} + \frac{2n-1}{2} \, f_{EOM} \right) \, \frac{2L}{c_0} + \Delta\phi \tag{A.61}$$

$$\varphi_{3a,even} = T_R \left( p \, f_{seed} + \left(p^2 + p + 2qp\right) \, \frac{f_{AOM}}{2} - n \, (2q+p) \, f_{EOM} \right)$$
$$- \left( f_{seed} + (q+p) \, f_{AOM} + \frac{2n-1}{2} \, f_{EOM} \right) \, \frac{2L}{c_0} + \Delta\phi \tag{A.62}$$

$$\varphi_{3b,odd} = T_R \left( p \, f_{seed} + \left(p^2 + p + 2qp\right) \, \frac{f_{AOM}}{2} - (2n-1) \left(q + \frac{p}{2}\right) f_{EOM} \right)$$
$$+ \left( f_{seed} + (q+p) \, f_{AOM} + \frac{2n-1}{2} \, f_{EOM} \right) \, \frac{2L}{c_0} - \Delta\phi \tag{A.63}$$

$$\varphi_{3b,even} = T_R \left( p \, f_{seed} + \left(p^2 + p + 2qp\right) \, \frac{f_{AOM}}{2} - n \, (2q+p) \, f_{EOM} \right)$$
$$+ \left( f_{seed} + (q+p) \, f_{AOM} + n \, f_{EOM} \right) \, \frac{2L}{c_0} - \Delta\phi \tag{A.64}$$

We can see that the beat frequencies are the same in each term. They are a multiple of $f_{AOM}$ plus or minus a multiple of $f_{EOM}$. The phase terms are different for the three terms $I_1$, $I_2$, and $I_3$.

# Bibliography

[1] Y. Oike, M. Ikeda, A. Asada, "Design and Implementation of Real-Time 3-D Image Sensor with 640 480 Pixel Resolution", *IEEE Journal of Solid-State Circuits*, Volume 39, pp. 622-628 (2004)

[2] A. Nemecek, K. Oberhauser, H. Zimmermann, "Distance Measurement Sensor With PIN-Photodiode and Bridge Circuit", *IEEE Sensors Journal*, Volume 6, pp. 391-397 (2006)

[3] G. Zach, H. Zimmermann, "A 2x32 Range-Finding Sensor Array with Pixel-Inherent Suppression of Ambient Light up to 120klx", *IEEE ISSCC*, (2009), pp. 352–353

[4] G. Zach, M. Davidovic, H. Zimmermann, "Extraneous-light resistant multipixel range sensor based on a low-power correlating pixel-circuit", *IEEE ESSCIRC*, pp. 236-239 (2009)

[5] C.C. Liebe, S. Dubovitsky, R. Peters, "3D Metrology Camera", *IEEE Aerospace Conference*, pp. 1-8 (2007)

[6] I. Coddington, W. C. Swann, L. Nenadovic, N. R. Newbury, "Rapid and precise absolute distance measurements at long range", *Nature Photonics*, Volume 3, pp. 351-356 (2009)

[7] P.D. Hale, F.V. Kowalski, "Output Characterization of a Frequency Shifted Feedback Laser: Theory and Experiment", *IEEE Journal of Quantum Electronics*, Volume 26, pp. 1845-1851 (1990)

[8] I.C.M. Littler, J.H. Eschner, "The cw modeless laser: model calculations of an active frequency shifted feedback cavity", *Optics Communications*, Volume 87, pp. 44-52 (1992)

[9] I.C.M. Littler, S. Balle, K. Bergmann, "The cw modeless laser: spectral control, performance data and build-up dynamics", *Optics Communications*, Volume 88, pp. 514-522 (1992)

[10] G. Bonnet, S. Balle, T. Kraft, K. Bergmann, "Dynamics and self-modelocking of a titanium-sapphire laser with intracavity frequency shifted feedback", *Optics Communications*, Volume 123, pp. 790-800 (1996)

[11] M. Stellpflug, G. Bonnet, B.W. Shore, K. Bergmann, "Dynamics of frequency shifted feedback lasers: simulation studies", *Optics Express*, Volume 11, pp.2060-2080 (2003)

[12] Koichiro Nakamura, Fumitoshi Abe, Kumio Kasahara, Takefumi Hara, Manabu Sato, Hiromasa Ito, "Spectral Characteristics of an All Solid-state Frequency-Shifted Feedback Laser", *IEEE Journal of Quantum Electronics*, Volume 33, pp. 103-111 (1997)

[13] K. Nakamura, T. Miyahara, H. Ito, "Observation of a highly phase-correlated chirped frequency comb output from a frequency-shifted feedback laser", Applied Physics Letters, Volume 72, pp. 2631-2633 (1998)

[14] K. Nakamura, T. Miyahara, M. Yoshida, T. Hara, H, Ito, "A New Technique of Optical Ranging by a Frequency-Shifted Feedback Laser", *IEEE Photonics Technology Letters*, Volume 10, pp. 1772-1774 (1998)

[15] K. Nakamura, T. Hara, M. Yoshida, Toshiharu Miyahara, Hiromasa Ito, "Optical Frequency Domain Ranging by a Frequency-Shifted Feedback Laser", *IEEE Journal of Quantum Electronics*, Volume 36, pp. 305-316 (2000)

[16] M. F. Brandl, "Investigation on Distance Measurement with Chirped Laser Light", diploma thesis in electrical engineering, *University of Technology, Vienna* (2010)

[17] L.P. Yatsenko, B.W. Shore, K. Bergmann, "Ranging and interferometry with a frequency shifted feedback laser", *Optics Communications*, Volume 242, pp. 581-598 (2004)

[18] V.V. Ogurtsov, L.P. Yatsenko, V.M. Khodakovskyy, B.W. Shore, G. Bonnet, K. Bergmann, "High accuracy ranging with $Yb^{3+}$-doped fiber-ring frequency-shifted feedback laser with phase-modulated seed", *Optics Communications*, Volume 266, pp. 266-273 (2006)

[19] V.V. Ogurtsov, L.P. Yatsenko, V.M. Khodakovskyy, B.W. Shore, G. Bonnet, K. Bergmann, "Experimental characterization of an $Yb^{3+}$-doped fiber ring laser with frequency-shifted feedback", *Optics Communications*, Volume 266, pp. 627-637 (2006)

[20] V.V. Ogurtsov, V.M. Khodakovskyy, L.P. Yatsenko, B.W. Shore, G. Bonnet, K. Bergmann, "An all-fiber frequency-shifted feedback laser for optical ranging; signal variation with distance", *Optics Communications*, Volume 281, pp. 1679-1685 (2008)

[21] L.P. Yatsenko, B.W. Shore, K. Bergmann, "Theory of a frequency-shifted feedback laser", *Optics Communications*, Volume 236, pp. 183-202 (2004)

[22] L.P. Yatsenko, B.W. Shore, K. Bergmann, "Coherence in the output spectrum of frequency shifted feedback lasers", *Optics Communications*, Volume 282, pp. 300-309 (2009)

[23] M. F. Brandl, O. D. Mücke, "Narrow-linewidth chirped frequency comb from a frequency-shifted feedback Ti:sapphire laser seeded by a phase-modulated single-frequency fiber laser", *Optics Letters*, Volume 35, pp. 4223-4225 (2010)

[24] M.M. Fejer, G.A. Magel, D.H. Jundt, R.L. Byer, "Quasi-Phase-Matched Second Harmonic Generation: Tuning and Tolerances", *IEEE Journal of Quantum Electronics*, Volume 28, pp. 2631-2654 (1992)

[25] D.S. Hum, M.M. Fejer, "Quasi-phasematching", *C.R. Physique*, Volume 8, pp. 180-198 (2007)

[26] W.S. Read, R. G. Turner, "Tracking Heterodyne Detection", *Applied Optics*, Volume 4, Issue 12, pp. 1570-1573 (1965)

# List of Abbreviations

| | |
|---|---|
| 3D | three-dimensional |
| AOM | acousto-optical modulator |
| AOFS | acousto-optical frequency shifter |
| BS | beam splitter |
| BW | bandwidth |
| DC | direct current |
| DFB | distributed feedback |
| EOM | electro-optical modulator |
| FC/APC | fiber connector / angle polished connector |
| FI | Faraday isolator |
| FSF | frequency-shifted feedback |
| FSR | free spectral range |
| FWHM | full width half maximum |
| NBW | noise bandwidth |
| OFDR | optical frequency domain ranging |
| QPM | quasi-phase matching |
| PD | photodiode |
| PM | phase modulation |
| PPLN | periodically poled lithium niobate |
| RF | radio frequency |
| SFL | single-frequency laser |
| SHG | second harmonic generation |
| SNR | signal-to-noise ratio |
| TiSa | titanium sapphire |
| VSG | Vector Signal Generator |

# Publications

## Peer-reviewed journal article

M. F. Brandl, O. D. Mücke, "Narrow-linewidth chirped frequency comb from a frequency-shifted feedback Ti:sapphire laser seeded by a phase-modulated single-frequency fiber laser", *Optics Letters*, Volume 35, pp. 4223-4225 (2010)

## Presentation at international conference

M. F. Brandl and O. D. Mücke, "Narrow-Linewidth Chirped Frequency Comb from a Seeded Frequency-Shifted Feedback Ti:Sapphire Lasers", talk CWH6, *Conference on Lasers and Electro-Optics (CLEO)*, Baltimore, MD, USA, May 1-6, 2011

# Acknowledgments

I would like to thank the people involved in this project for their support.

- **Andrius Baltuška** for giving me the opportunity to build the laser with his group's equipment, and for the support by him and his team.

- **Alma Fernández González** for providing the 3mm TiSa crystal from her stock.

- **Oliver Mücke** for introducing me in building lasers, for support in the theoretical model as well as building the laser, for his guidance in the scientific work, and for his feedback in writing this thesis.

- **Audrius Pugzlys** for his help and support in building the laser.

- **Robert Swoboda** for his support with the equipment that was needed to build the laser and to do the measurement.

- **Horst Zimmermann** for giving me the opportunity to work at this topic and for his trust and support during the construction of the laser.

- **Family and friends** for their support.